Localization and Mitigation of Loss in Niobium Superconducting Circuits

M. Virginia P. Altoé,[1,†] Archan Banerjee,[2,3,†] Cassidy Berk,[1,†] Ahmed Hajr,[2,4,5,†]
Adam Schwartzberg,[1] Chengyu Song,[1] Mohammed Alghadeer,[6] Shaul Aloni,[1] Michael J. Elowson,[1]
John Mark Kreikebaum,[2,3] Ed K. Wong,[1] Sinéad M. Griffin,[1,3] Saleem Rao,[6]
Alexander Weber-Bargioni,[1] Andrew M. Minor,[1,7] David I. Santiago,[2,4] Stefano Cabrini,[1]
Irfan Siddiqi,[2,3,4] and D. Frank Ogletree[1,*]

[1] *Molecular Foundry Division, Lawrence Berkeley National Laboratory, Berkeley, California 94720, USA*
[2] *Quantum Nanoelectronics Laboratory, Department of Physics, University of California at Berkeley, Berkeley, California 94720, USA*
[3] *Materials Sciences Division, Lawrence Berkeley National Laboratory, Berkeley, California 94720, USA*
[4] *Computational Research Division, Lawrence Berkeley National Laboratory, Berkeley, California 94720, USA*
[5] *Graduate Group in Applied Science and Technology, University of California at Berkeley, Berkeley, California 94720, USA*
[6] *Department of Physics, King Fahd University of Petroleum and Minerals, Dhahran 31261, Kingdom of Saudi Arabia*
[7] *Department of Materials Science and Engineering, University of California at Berkeley, Berkeley, California 94720, USA*

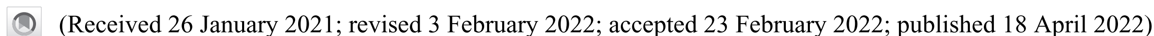
(Received 26 January 2021; revised 3 February 2022; accepted 23 February 2022; published 18 April 2022)

Materials imperfections in planar superconducting quantum circuits—in particular, two-level-system (TLS) defects—contribute significantly to decoherence, ultimately limiting the performance of quantum computation and sensing. The identification of specific parasitic layers and their associated loss contributions has, however, proven elusive. Using a combination of x-ray photoemission spectroscopy (XPS) and analytical scanning transmission electron microscopy (STEM), we determine the thickness, chemical composition, and location of the oxides present in niobium-on-silicon coplanar-waveguide (CPW) resonators and quantify their respective contributions to the measured single-photon quality factor (Q). Using selective chemical etching, we reduce first the substrate-air oxide then the metal-air oxide thickness, dramatically reducing both TLS (δ_{TLS}) and non-TLS (δ_{hi}) losses, resulting in a median Q value over 5×10^6, with individual devices approaching 6×10^6. We find that silicon surface oxides host 70% of TLS losses, with a $\delta_{\mathrm{TLS}} : \delta_{\mathrm{hi}}$ loss-density ratio near 11:1. In contrast, niobium surface oxides host 77% of non-TLS losses, uniformly distributed within the oxide layer, with a $\delta_{\mathrm{TLS}} : \delta_{\mathrm{hi}}$ loss-density ratio of 3:4 for the superconducting circuits investigated in this work. Only 7% of losses come from other sources, including the niobium-silicon interface, which is sufficiently clean in our devices to allow epitaxial Nb nucleation on Si. As we mitigate surface losses through selective modification of the interface dielectrics, we arrive in a regime where TLS losses are no longer dominant, which will allow other types of losses in superconducting circuits to be investigated in more detail, including nonequilibrium quasiparticles.

DOI: 10.1103/PRXQuantum.3.020312

I. INTRODUCTION

Rapid advances in hardware for quantum information processing (QIP) are bringing within reach quantum calculations that cannot be performed on classical computers [1]. However, in solid-state qubits and architectures using planar circuitry for quantum control, there remain two central hurdles to fully realize this quantum advantage: first, the current error rates for performing qubit logical operations need to be reduced and, second, these low error rates need to be maintained as larger-scale systems are made. A key source of fidelity loss in superconducting circuits, semiconductor quantum dots, and trapped-ion systems results from materials defects at surfaces and interfaces. While material and hardware specific, such decoherence channels plague all existing state-of-the-art QIP platforms [2]. Moreover, while efforts to maximize

*DFOgletree@LBL.gov
†These authors contributed equally to this work.

Published by the American Physical Society under the terms of the Creative Commons Attribution 4.0 International license. Further distribution of this work must maintain attribution to the author(s) and the published article's title, journal citation, and DOI.

the performance of imperfect hardware via algorithm and architecture codesign [3–7] are important to near-term progress, fully understanding and controlling material and environmental losses is a fundamental materials challenge [2,8,9], critical for the deployment of robust quantum solutions. An analogy can be made with the development of classical computing, where decades of research in semiconductor physics, advanced materials engineering, and process development has been required to realize processor chips with 10×10^9 transistors operating at gigahertz frequencies. Likewise, materials characterization, fabrication, and understanding of existing and new QIP materials will be necessary as we traverse the noisy-intermediate scale quantum (NISQ) era toward fully fault-tolerant scalable quantum computers.

Superconducting qubits are one of the most mature and well-studied hardware platforms for QIP [10,11] and proof-of-principle experiments have demonstrated both "quantum advantage" [12] in computation and "break-even" error correction [13]. The basic superconducting-circuit building block is a nonlinear quantum oscillator (qubit) coupled to a quantum harmonic oscillator (resonator), which enables quantum nondemolition measurements of the qubit state through circuit QED (quantum electrodynamics) [6,14,15]. Qubits are commonly realized as lithographically patterned planar devices on silicon or sapphire substrates, consisting of Al-AlO_x-Al Josephson junctions shunted by capacitive (e.g., transmon) or inductive (e.g., fluxonium) circuit elements. The nonjunction conductors are often aluminum but other elemental or compound superconductors are also used, including Nb, Ta, TiN, NbN, and NbTiN. A commonality between these materials is the presence of oxide films, which either form during fabrication processes, such as oxygen plasma cleaning, or in ambient conditions after fabrication.

It is broadly recognized that the dominant loss mechanism for superconducting circuits is from coupling to two-level-system (TLS) defects in the amorphous dielectric films at interfaces, including the Josephson-junction oxide itself [16,17]. For this reason, it is critical to understand the nature of these oxides and their specific contributions to TLS and other loss processes. Conceptually, a TLS is an atomic scale defect with two energetically similar configurations (states) separated by an activation barrier. Thermally activated transitions are suppressed at the millikelvin operating temperature of quantum circuits but quantum tunneling between the states can occur on experimental time scales. TLS ensembles will have a wide distribution of energy splittings, barrier heights, and tunneling rates due to the structural disorder of amorphous materials. TLSs were first proposed to explain the anomalous heat capacity of glassy materials at temperatures below a few kelvin, leading to the development of the "standard tunneling model" [18]. Despite years of investigation, the microscopic nature of TLSs remains unknown, although a number of models have been proposed, including interstitial hydrogen, bistable dangling bonds, and collective motions of multiple atoms. The role of TLSs in quantum decoherence has recently been reviewed in depth [19], along with experimental work correlating decoherence with materials and processing [20] and mitigation strategies for quantum decoherence [21].

When TLSs are resonant with the microwave frequencies of quantum circuits, they can couple to fluctuating electric fields associated with circuit operation, causing decoherence and information loss. As the circuit power and the electric field strength increase, resonant TLSs become strongly coupled, reducing loss and increasing coherence. Saturation allows power-dependent TLS losses to be distinguished from other power-independent loss mechanisms, including nonequilibrium quasiparticles and magnetic flux noise [19,22].

A key remaining challenge is to understand the specific chemical and structural composition of each interfacial layer in a functional quantum device and relate this to quantum decoherence in the system. Such detailed information is vital to improve processing protocols to mitigate the surface losses and, ultimately, to gain fundamental understanding by correlating specific materials with microscopic mechanisms for TLSs and other decoherence processes.

In this work, we experimentally investigate surface-oxide properties and their contributions to the loss observed in superconducting coplanar-waveguide (CPW) resonators in the single-quantum regime. We develop chemical-etching techniques to selectively remove the oxides, first on the insulating silicon substrate and then on niobium circuit elements. Subsequent to electronic characterization, resonators are analyzed using x-ray photoemission spectroscopy (XPS) and scanning transmission electron microscopy (STEM) to determine the thickness, chemical composition, and structure of the exposed oxide layers. This process is repeated on multiple test chips cut from a single wafer and over a range of etch times. Our results demonstrate a systematic improvement in resonator Q, up to 6×10^6 with extended acid etching, which removes the silicon process oxide and then significantly reduces the thickness of the niobium process oxide. In this way, we are able to localize a significant majority of both power-dependent TLS and power-independent non-TLS losses to different interfaces while mitigating their impact on circuit performance.

II. EXPERIMENTAL APPROACH

CPW resonators are a central component in many superconducting qubit architectures and provide a flexible standalone vehicle for characterizing microwave-frequency materials losses in the single-quantum excitation regime. Our chip design is comprised of a 10 mm $\times$ 10 mm square

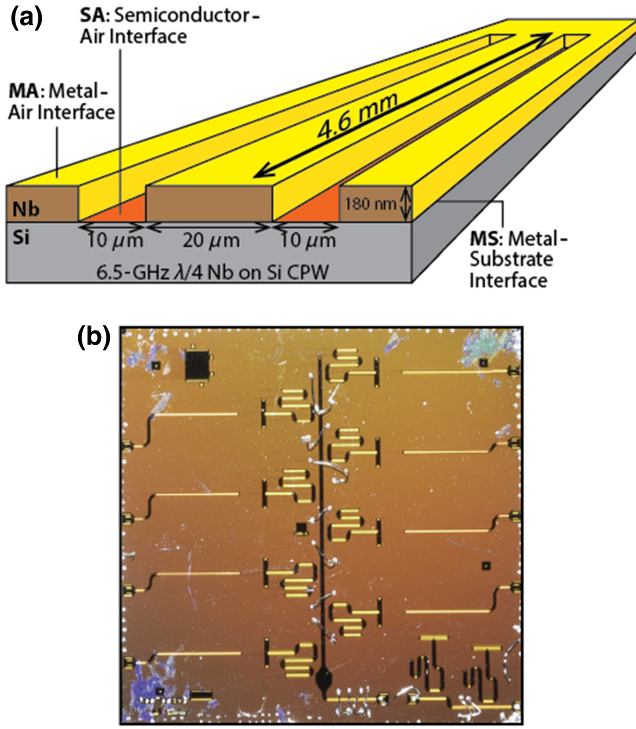

FIG. 1. (a) A sketch of the λ/4 CPW resonators used in this study. The frequencies range from 6 to 7 GHz and a 6.5-GHz approximately 50-Ω resonator is 4.6 mm long, grounded at one end and open at the other. The center conductor is 20 μm wide with 10-μm insulating gaps. The Nb superconducting layer is approximately 180 nm thick and the substrate is high-resistivity Si(100). The material interfaces are indicated. (b) An optical image of a 10 mm × 10 mm Nb-on-Si resonator test chip after cryogenic loss measurements, showing the central vertical readout line with four resonators on each side. The horizontal traces from the left and right edges would have been control lines on an eight-qubit chip. Two additional resonators are included at the lower right. The Nb ground plane has 2 μm × 2 μm square magnetic flux traps etched through the Nb on a 10-μm grid.

silicon (100) substrate with ten λ/4 approximately 50-Ω resonators in the 6-GHz frequency band capacitively coupled to a single frequency-multiplexed readout line, shown in Fig. 1. We characterize ten such chips (two used as a standard reference and eight subjected to acid etching) derived from a single 150-mm-diameter wafer.

Our resonator fabrication involves chemical substrate cleaning, magnetron sputter deposition of the approximately 180-nm-thick niobium layer, electron-beam lithography and reactive-ion etching to define circuits, and plasma ashing to remove resist residues—typical of our qubit-fabrication process detailed previously [23]. The wafer is then protected with a new resist film before chip dicing and storage until use. Samples are stored and transported under vacuum between steps (for details, see Appendix A). Each chip goes through a testing cycle involving: (i) wet-chemical-resist stripping; (ii) acid etching for variable intervals; (iii) XPS measurements on each resonator; (iii) wire bonding and packaging of the test chip in a shielded sample box; (iv) millikelvin-temperature coherent-microwave characterization of power and temperature-dependent performance; and (v) finally, postmeasurement characterization by XPS and STEM.

Resonator losses are characterized by microwave reflectometry of the frequency-multiplexed test-chip resonators. The observed total quality factor $Q_T = f_0/\Delta f = \delta_T^{-1}$, where f_0 and Δf are the measured resonant frequency and the line width at half maximum and δ_T is the total loss tangent, including energy lost to the 50-Ω input feed line ($\delta_{\text{ext}} = 1/Q_{\text{ext}}$) and internal dissipation ($\delta_{\text{int}} = 1/Q_{\text{int}}$). Fits to resonator transmission are consistent with $Q_{\text{ext}} \sim 0.7 \times 10^6$, in good agreement with electromagnetic simulations. Appendix H describes the cryogenic measurement setup and resonance fitting.

In our discussion, we follow a common practice in the literature [16,20,24,25] and decompose the measured resonator internal dissipation $\delta_{\text{int}} = \delta_{\text{TLS}} + \delta_{\text{hi}}$ into a power-dependent "TLS" component δ_{TLS} and a power-independent or high-power component δ_{hi}. We define δ_{hi} as the loss when the resonator is excited with 10^7 microwave photons and δ_{TLS} as the single-photon loss less δ_{hi} [see Fig. 6(b)].

III. ANALYSIS OF STANDARD RESONATOR INTERFACES

CPW resonators and other quantum circuit elements are not ideal and are generally assumed to have amorphous dielectric films at the substrate-air (SA), superconducting metal-air (MA), and metal-substrate (MS) interfaces, which host TLSs and are the major source of decoherence. These films include: surface oxides of Si, Al, and Nb; substrate contamination or damage due to cleaning during fabrication; and organic residues from lithography; as well as adsorbates from air exposure or condensed during cryogenic cool-down for air-vacuum interfaces.

Our standard Nb resonators show high performance and are similar in structure and fabrication to the resonators on multiqubit chips produced in Berkeley [23]. Their losses are comparable to the state of the art for planar niobium resonators, based on McRae's 2020 resonator review [20], with median single-photon resonator quality factor $Q_{\text{int}} = 0.93 \times 10^6$ ($Q_{\text{TLS}} = 1.30 \times 10^6$) for the 20 resonators on our two test chips. In this section, we present a detailed analysis of the standard resonator interfaces and materials. In the next section, we analyze the effect of etching on resonator performance and correlate this with changes in interface properties.

The standard resonator silicon and niobium surface oxides are process oxides, formed during resonator fabrication. The SA interface and niobium sidewalls are

reactive-ion etched during fabrication. The MA interface is covered by photoresist for electron-beam lithography. Both interfaces are subjected to chemical-resist stripping before being covered with a second protective polymer layer prior to dicing the wafer into individual test chips. The fabricated devices are stable for many months when protected by the polymer layer used for storage, or for many days in ambient conditions. This protective polymer is chemically stripped, followed by plasma ashing to remove organic residues before resonator performance testing and materials analysis (for process details, see Appendix A).

The classical Cabrera-Mott model describes metal oxidation under ambient conditions [26,27] as oxygen atoms move through the growing oxide driven by the electric field resulting from the work-function difference between the metal and the exposed oxide surface. On many surfaces, including Al and Si, oxidation slows dramatically once the film is a few nanometers thick. Oxidation may be faster during resonator fabrication due to surface charging under plasma conditions or in the presence of ionizing radiation [28]. Oxygen radicals and ions can react with the surface in addition to molecular oxygen and stronger electric fields are present. As we show below, process oxides and ambient or native oxides have different impacts on decoherence in quantum circuits.

Figure 2 shows a typical STEM cross section of a niobium-on-silicon CPW resonator fabricated in the Quantum Nanoelectronics Laboratory (QNL). This is essentially the QNL "eight-qubit ring" layout without the qubits, and similar qubits and resonators are in active use [23,29,30]. The thin slice is lifted out after focused-ion-beam machining and shows the edge of the insulating gap where Nb has been plasma etched away. Cross sections are aligned with the (011) plane of the Si(100) substrate so that TEM images can be acquired on the Si[011] zone axis. Nb is over-etched by approximately 75 nm to ensure that there are no disconnected Nb islands remaining in the insulating gaps, which can degrade performance. Such islands have been identified on other devices with AFM and nano-Auger analysis (not shown). Chemical analysis by STEM EDS and electron-energy-loss spectroscopy (EELS) shows the MA and SA surface oxides. The process oxide is thicker on Nb than on Si. The MS interface is clean, with only Si and Nb at the interface and oxygen below detection limits. No carbon is detected at any interface. We now present an atomic scale analysis of each interface.

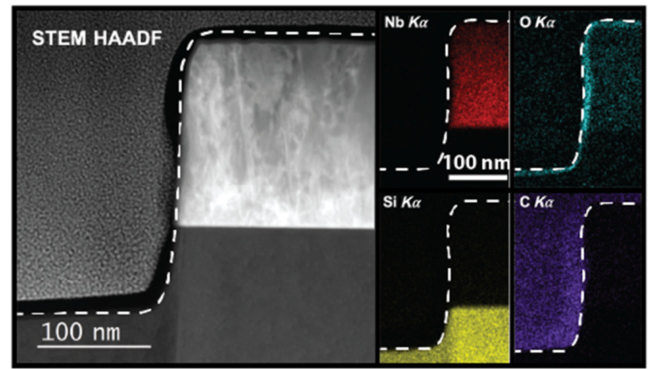

FIG. 2. A STEM cross-section image of a standard (nonetched) Nb-Si resonator. The high-angle annular dark-field image on the left maps large-angle electron-scattering intensity, which increases with the atomic number Z. The bright area is the Nb film and the contrast variation reflects dislocations and grain boundaries in the sputtered film. The black border and the speckled region on the left are, respectively, the carbon and platinum layers deposited during sample preparation. The uniform gray area below is the Si(100) substrate. The dashed white lines separate the resonator surface from the deposited layers. The "blurring" of the Nb sidewall is due to the projection of the surface roughness through the approximately 50-nm-thick cross-section lamella. The thin gray layers next to the protective carbon are the Nb and Si surface oxides. The elemental energy-dispersive spectroscopy (EDS) maps on the right show the Nb, O, Si, and C distributions. The thicker Nb and thinner Si surface oxides are clearly visible in the O map. (During sample preparation, monolayer amounts of oxygen and carbon can absorb on the freshly exposed surfaces of the lamella.)

A. The niobium MA interface

The niobium process oxide is shown in detail in Fig. 3(a), a characteristic TEM image showing the top of columnar Nb grains with approximately 5 nm of amorphous niobium oxide with significant roughness (approximately 1 nm) due to the niobium grain structure (See also Appendix G and Fig. 17). Figure 3(b) shows the oxide elemental composition. This STEM-EELS map of the Nb:(Nb + O) atomic ratio is acquired with a 0.1-nm-diameter probe, using the Nb $M_{4,5}$ edge and the O K edge. The map reveals the NbO_x composition gradient, showing the transition from metallic Nb through increasingly oxidized phases to Nb_2O_5 at the air interface. The O:Nb ratio increases moving toward the top surface as the dominant Nb oxidation state changes from +2 to +4 to +5. The associated EELS spectra (Appendix G) are consistent with the observed phases [31,32]. No oxygen is detected at Nb grain boundaries in our films, although this has been reported for films grown in different conditions [33].

Figure 3(c) shows the Nb_{3d} XPS peak region with the spin-orbit split Nb $3d_{3/2}$: $3d_{5/2}$ doublets corresponding to different niobium oxidation states identified by peak fitting (see details in Appendix F). The exposed resonator surface is analyzed by XPS before cross-section preparation and the Nb surface composition is averaged over several approximately 400-μm-diameter regions for each resonator on the chip. Spatially averaged XPS complements the atomic resolution TEM thickness measurements of selected cross sections, allowing for a broad overview of the state of the metal-air

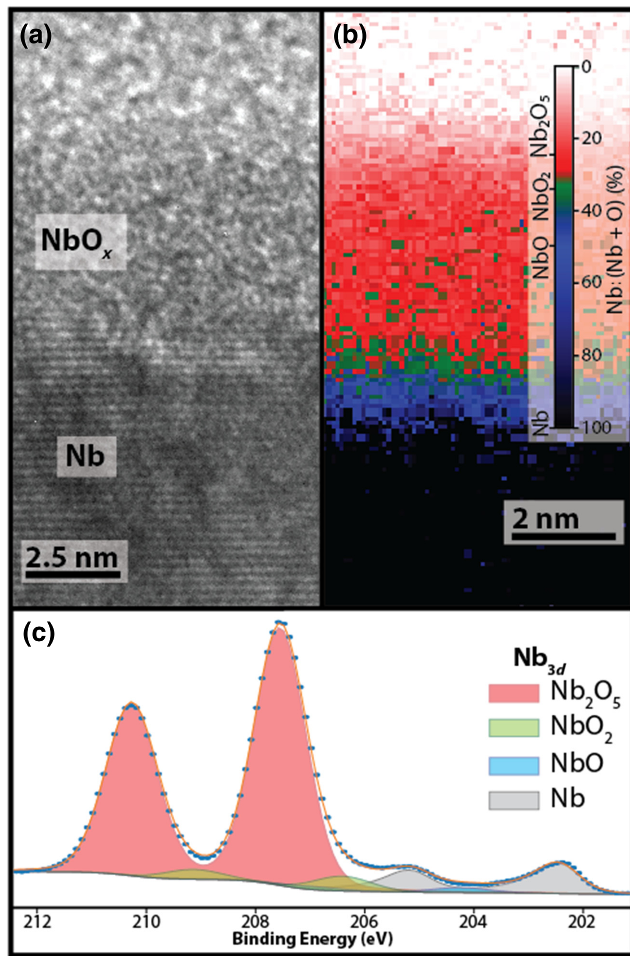

FIG. 3. The niobium metal-air (MA) interface. (a) A high-resolution TEM image showing the MA surface roughness and the approximately 4.8-nm NbO_x amorphous oxide. (b) A STEM-EELS map of variations in the Nb:(Nb + O) ratio within the oxide. (c) A Nb_{3d} XPS spectrum with peak fits to the different oxide components.

interface. The chemical shifts associated with the different oxidation states [34] are large enough to allow the individual contributions to be resolved through multicomponent fitting routines and provide a reliable determination of relative niobium oxide compound concentrations within the probed volume. Previous Nb XPS resonator studies have proposed a model with a niobium pentoxide surface layer and suboxides near the metal [33,35]. This model is confirmed by our spatially resolved EELS maps [Fig. 3(b), Fig. 17 and Appendix G]. The metallic Nb signal is attenuated by the oxide layers with a calculated attenuation length of 1.7 nm. The ratio of oxidized to metallic Nb peak areas gives a total oxide thickness of 4.8 ± 0.5 nm. Fits of the XPS data to a layered oxide attenuation model give 0.3 nm of NbO, 1.0 nm of NbO_2, and 3.5 nm of Nb_2O_5 (Appendix F).

B. The silicon SA interface

The niobium film covering the silicon wafer is patterned with electron-beam lithography and reactive-ion etching to expose the silicon surface, creating insulating gaps. The plasma etching, chemical-resist stripping, and plasma ashing produces a process-oxidized silicon surface modified from the standard native oxide, similar to the niobium process oxide discussed above. Figure 4(a) shows the silicon-air interface properties in TEM cross section. There is a sharp transition between the crystalline substrate and the approximately 3-nm-thick SiO_x amorphous oxide. The XPS spectrum and peak fits of the silicon surface are shown in Fig. 4(b). The Si_{2p} XPS peak region includes the spin-orbit split Si $2p_{1/2}$: $2p_{3/2}$ doublets from the crystalline substrate and a mixture of chemically shifted oxide doublets, including fully oxygen-coordinated Si^{4+} similar to bulk SiO_2 along with suboxides with mixed Si—Si and Si—O—Si bonding [36]. The median oxide thickness determined by XPS is $2.4^{+0.7}_{-0.3}$ nm.

C. The niobium MS interface

The Nb-Si interface is strikingly different from models commonly described in the literature, which assume an amorphous dielectric interface layer a few nanometers

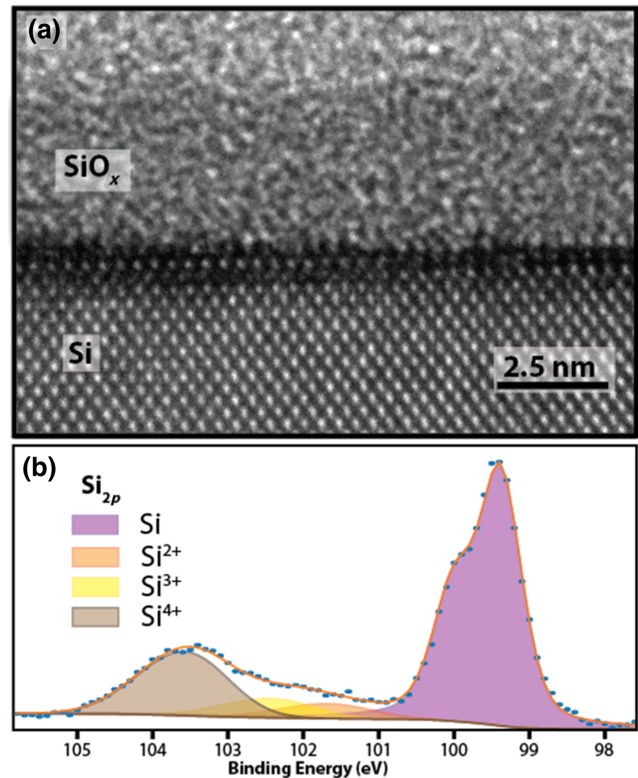

FIG. 4. The silicon substrate-air (SA) interface. (a) A high-resolution TEM image showing the crystalline Si(100) substrate and the amorphous surface oxide. (b) A Si_{2p} XPS spectrum, with the Si substrate signal attenuated by the surface oxides.

thick [20,24,25,37]. We find no evidence for an amorphous layer in multiple high-resolution TEM images of our resonators. Clean Al-Si resonator interfaces have been reported after substrate processing [38] or ultrahigh vacuum annealing and Al deposition [39]. TEM selected-area diffraction from MS interface cross-section samples shows epitaxial nucleation of the niobium grains that form the polycrystalline superconducting film (for details, see Appendix C). Epitaxial nucleation requires a clean interface—an amorphous interfacial layer would prevent epitaxial growth, since Nb nucleation would no longer be sensitive to the substrate crystallography. Some degree of local disorder, including TLS defects, could still be present at the Nb-Si interface.

IV. OXIDE ETCHING AND RESONATOR LOSSES

We use buffered oxide etch (BOE), a hydrofluoric acid–NH_4F solution widely used in semiconductor processing, for our resonator experiments (Appendix D). Our measured niobium oxide etch rate of approximately 3 pm/s (Fig. 14 and Appendix E) is hundreds of times slower than the 1.8-nm/s silicon oxide etch rate [40]. This large SiO_2:Nb_2O_5 etch selectivity, over 600:1 for 5:1 BOE, reflects differences in Nb and Si etch chemistry, and allows us to identify the resonator-loss contributions from the different interfaces, as well as their distribution within the niobium oxide, by varying etching times.

A 30-s etch in BOE should completely dissolve the few nanometers of SA silicon process oxide, while removing only a monolayer or so of the thicker MA niobium oxide layer. This is confirmed in Fig. 5(a). The initial $2.4^{+0.7}_{-0.3}$-nm process oxide, with a strong Si^{+4} component, is replaced by a thinner (0.8 ± 0.2)-nm oxide with almost no Si^{+4}. There is no obvious correlation between the SiO_x thickness and the etch time, consistent with removal of the process oxide followed by reoxidation (Appendix E; see also Table I). In contrast, changes to the MA niobium process oxide after 30 s are too small to detect, as they are smaller than sample-to-sample variations. The niobium oxide is monotonically reduced with longer etch times [Figs. 5(b), 5(c), and 17].

In Fig. 6, we compare internal losses from reflectometry data for unetched and etched resonators at 100 mK through resonance curves [Fig. 6(a)] and as a function of the photon number [Fig. 6(b)]. $\delta_{\rm int}$ is decomposed into the non-TLS

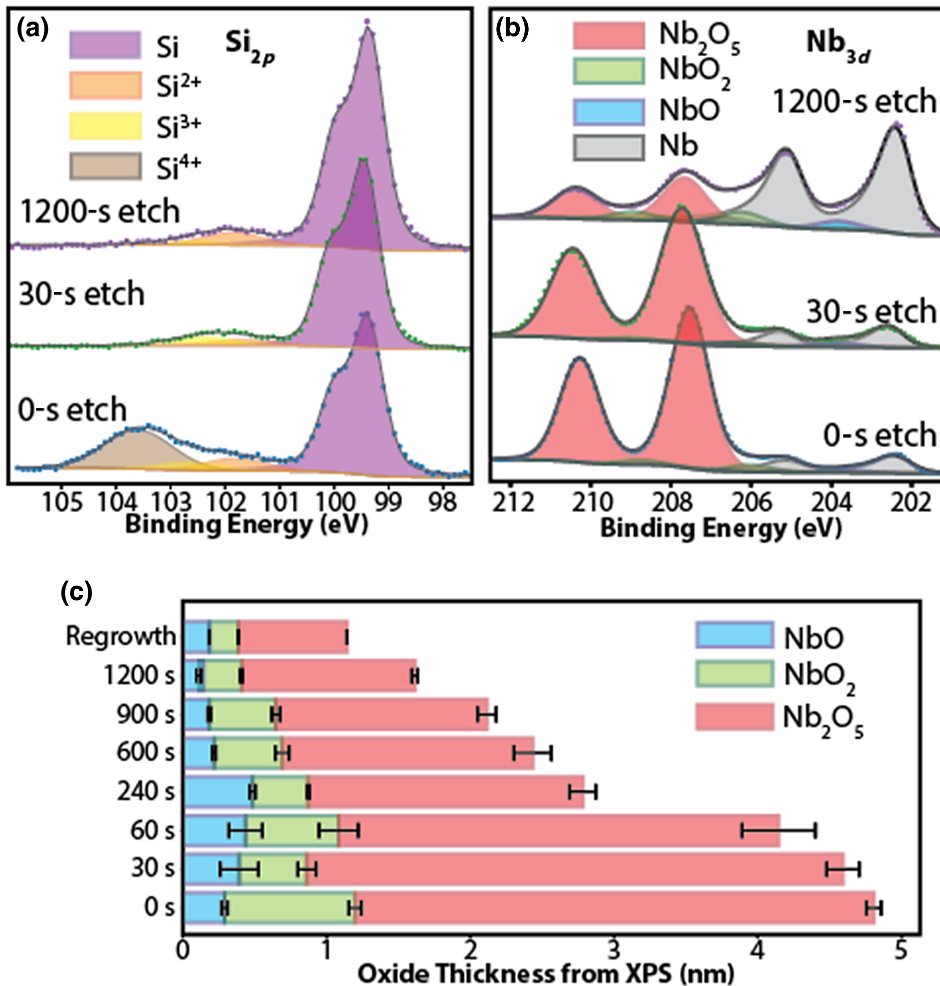

FIG. 5. XPS measurements of process oxides before etching, after 30 s, and after 1200 s of BOE etching. (a) The silicon $2p$ region showing the chemical transformation of SiO_x interface chemistry by etching. (b) The niobium $3d$ region. A 30 s etch leaves the oxide almost unchanged, while 1200 s significantly reduces the oxide thickness. The Nb suboxide contributions become more visible in the spectra as the thickness of the Nb_2O_5 overlayer is reduced (see Appendix F for details). (c) Steady reduction of the NbO_x thickness with increasing etch time. The top-bar "regrowth" comes from experiments discussed in Appendix E and Fig. 12. The other bars are resonator experiments. The NbO layer (blue, on the left) is closest to the Nb metal, while the Nb_2O_5 layer (red, on the right) is exposed to air. The error bars show point-to-point variations across each sample.

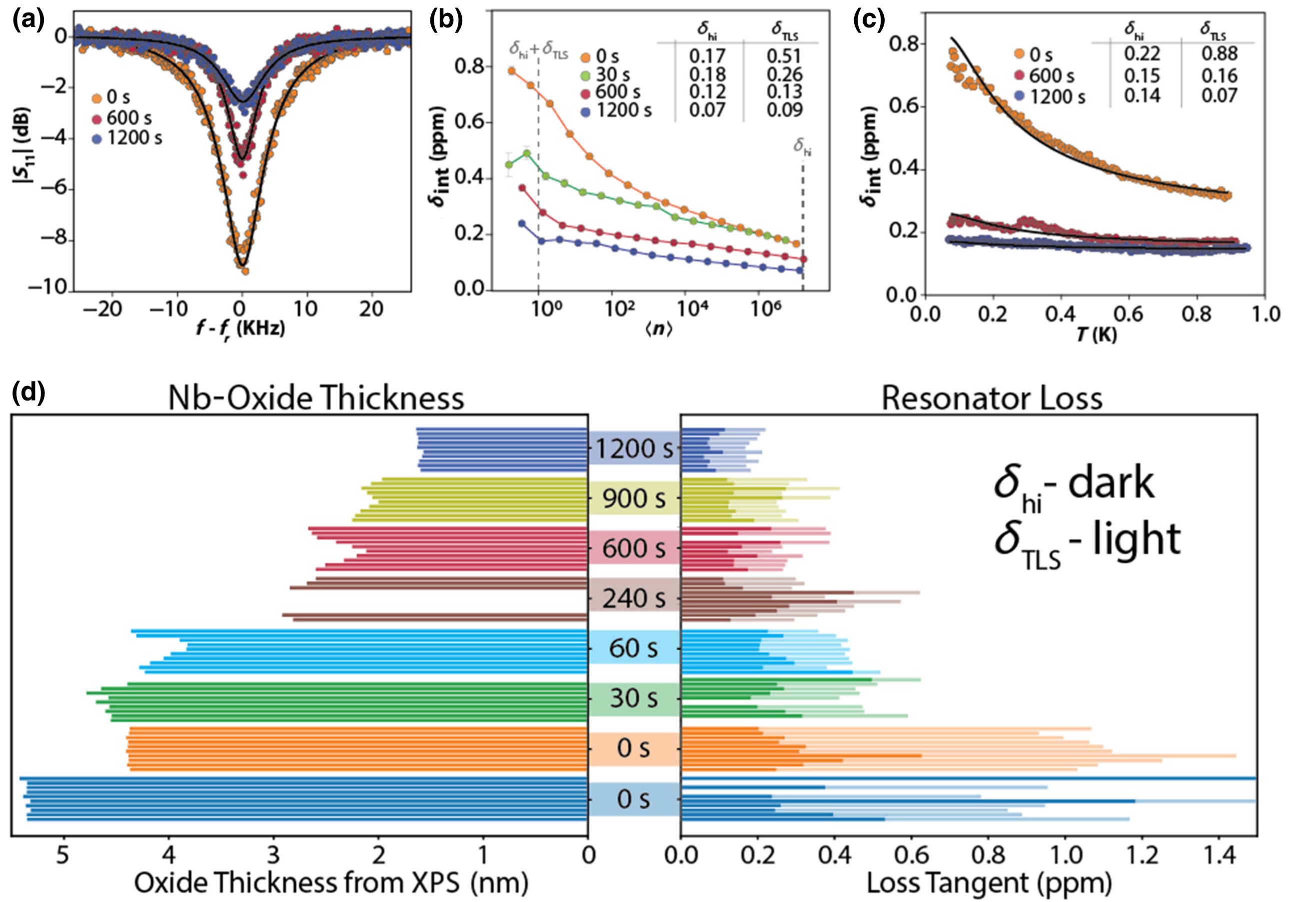

FIG. 6. (a)–(c) Microwave reflectometry comparing the lowest-loss resonators from unetched (orange), 600 s (red) and 1200 s (blue) etched chips. (a) Single-photon $|S_{11}|$ reflectometry. The decreased peak depth at resonance shows reduced loss. (b) The resonator intrinsic loss δ_{int} as a function of the photon number $\langle n \rangle$, decomposed into the 10^7-photon high-power loss δ_{hi} and the single-photon loss $\delta_{\text{hi}} + \delta_{\text{TLS}}$, as shown by the vertical dashed lines, yielding the values shown in the inset. Etched resonators show reduced losses at all power levels. (c) The temperature-dependent δ_{int} at $\langle n \rangle \approx 1$ fit to the TLS standard tunneling model (see Appendix H). The inset shows the thermal fitting results. (d) Grouped histograms correlating the resonator loss (right) and the NbO_x thickness from XPS (left) for all resonators using the method of (b). The light-colored bars show the TLS loss δ_{TLS} and the darker bars the high-power loss δ_{hi}, so the combined length is the measured single-photon loss. Unetched resonators (results from two different unetched "0 s" reference chips shown in blue and orange) are dominated by TLS losses, while δ_{TLS} and δ_{hi} are similar for etched resonators.

high-power loss δ_{hi} at $\langle n \rangle \sim 10^7$ and the single-photon loss $\delta_{\text{hi}} + \delta_{\text{TLS}}$ at $\langle n \rangle \sim 1$. The temperature dependence of the single-photon loss [Fig. 6(c)] gives an independent estimate of δ_{TLS} and δ_{hi}, consistent with, but not identical to, the values derived from the photon-number dependence. The histograms in Fig. 6(d) show the correlation between the NbO_x thickness and the losses. For unetched resonators, we find a median δ_{TLS} of $0.77^{+0.04}_{-0.12}$ ppm and δ_{hi} of $0.31^{+0.10}_{-0.06}$ ppm. Unetched test chips show larger variations in individual resonator performance, which could be due to lithographic resist residues, which are also mitigated by BOE etching. δ_{int} decreases with the etch time, reaching a test-chip single-photon median δ_{TLS} of 0.11 ± 0.00 ppm, an 86% reduction, and δ_{hi} of $0.08^{+0.02}_{-0.00}$ ppm, a 74% reduction. The TLS losses are similar to the non-TLS losses at the longest etch times and the best-performing etched resonators have quality factors Q_{int} over 6×10^6.

V. DISCUSSION

Through selective etching, we show that the silicon oxide at the SA interface hosts approximately 70% of the resonant TLSs that limit resonator performance. Figure 7(a) illustrates the loss changes resulting from BOE etching. The initial 30-s etch removes the original SA SiO_2 process oxide while dissolving only an estimated 100 pm of the MA Nb_2O_5. There is also a modest approximately 17% reduction in non-TLS loss. After etching, a new, ambient silicon oxide forms when the sample is exposed to air during sample mounting and before cryogenic loss

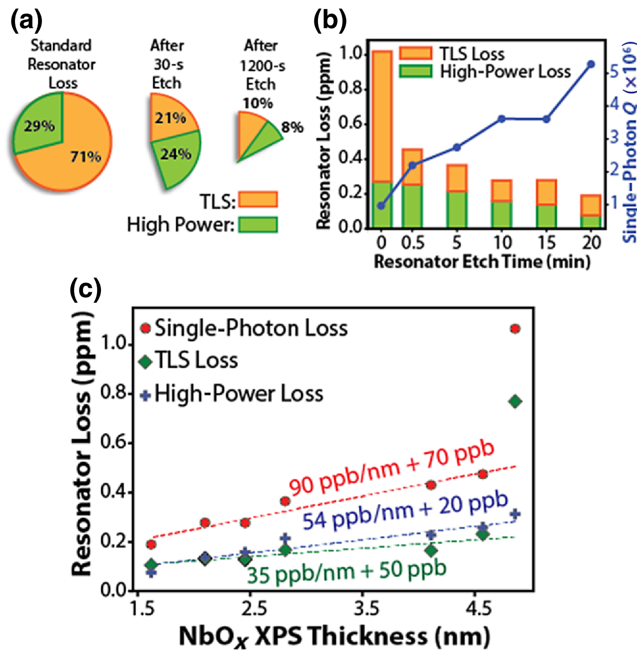

FIG. 7. (a) Pie plots comparing the loss distributions before and after etching. TLS losses dominate standard resonators, while non-TLS losses become more important with etching. The shortest etch reduces the total loss by half, while a 1200-s etch reduces the loss more than fivefold. (b) The resonator loss components and the quality factor as a function of the etch time (note the nonlinear x axis). (c) Linear fits to loss components versus the NbO_x thickness. The $\delta_{TLS} : \delta_{hi}$ loss-density ratio is 3:4. The residual δ_{TLS} and δ_{hi} losses extrapolated to zero thickness are 50 and 20 ppb, respectively, compared to starting values of 770 and 310 ppb.

measurements (Appendix A, E). The regrown SiO_x thickness varies between 0.2 and 2 nm (Table I), with no obvious correlation with either the etching time or loss. The ambient oxide is thinner and chemically different from the original process oxide formed in dry conditions, as shown in Fig. 5(a). The process oxide is primarily in the 4+ oxidation state, indicating Si bonding to four bridging O atoms, as in bulk SiO_2. Bulk Si has four Si—Si bonds. The regrown oxide is a mixture of Si in the 2+ and 3+ oxidation states, corresponding to two or three bridging oxygen bonds and two or one Si—Si bonds, respectively. This chemically different regrown oxide must have a significantly lower resonant TLS concentration than the original process oxide to be consistent with our loss data. This suggests that hydroxyl groups, expected with ambient oxidation but not with dry-process oxidation, may not be a strong contributor to the TLS losses in resonator thin film dielectrics and that Si^{4+} bonding motifs could be important in thin-film loss, even though OH is known to increase the TLS density in bulk silica [18].

Selective etching shows that the niobium MA process oxide hosts the majority of the non-TLS losses and that these losses are uniformly distributed throughout the

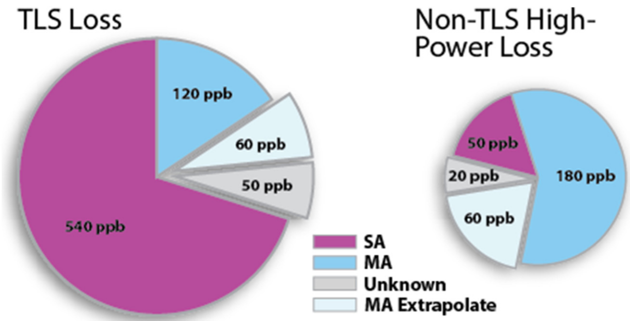

FIG. 8. The localization of 93% of both the TLS and the non-TLS loss through selective etching. The loss reduction in standard resonators due to SA etching (magenta) and MA etching (blue). The projected loss reduction from complete MA-oxide removal (light blue) extrapolated from fits in Fig. 7(c). The non-localized loss (unknown, in gray) includes contributions from the MS interface, the regrown SA oxide, and loss associated with bulk Si and Nb. The pie areas represent δ_{TLS} and δ_{hi} in parts per billion (ppb).

thickness of the interface oxide. Figure 7(b) shows the initial sharp drop in δ_{TLS} as the SA oxide is etched away, followed by a continuous decrease in the TLS and non-TLS losses with the MA etch time. The fits in Fig. 7(c) show the linear dependence of both δ_{TLS} and δ_{hi} on the NbO_x thickness. The rightmost points are unetched resonators, the standard-loss baseline. The large drop in δ_{TLS} with the minimum 30-s etch reveals the outsized impact of silicon oxide on the loss mechanisms (see also Appendix I). Extrapolation to zero niobium oxide would mean that the residual TLS and high-power losses from all other sources are approximately 50 and 20 ppb, respectively. If we attribute the extrapolated δ_{TLS} and δ_{hi} contributions to the MA interface, we are now able to localize all but approximately 7% of the resonator losses to the oxidized surface of the resonator, as shown in Fig. 8. Our clean Nb-Si MS interface contributes to the dominance of surface-oxide losses. Woods has reported MS loss contributions as high as 20% for some TiN-Si resonator geometries [25]. The "unknown" regions are some combination of losses from the MS interface, the regrown SA silicon oxide, and noninterfacial sources of loss including trapped vortexes and nonequilibrium quasiparticles [41,42] as well as loss associated with the bulk Nb superconductor and the Si substrate.

Silicon surface-oxides host 70% of the TLS loss and only 16% of the non-TLS loss, with a $\delta_{TLS} : \delta_{hi}$ loss-density ratio of almost 11:1. In contrast, niobium surface-oxides host 23% of the TLS loss and 77% of the non-TLS loss, with a $\delta_{TLS} : \delta_{hi}$ loss-density ratio of 3:4 for the superconducting circuits investigated in this work. We also see a clear loss difference between silicon process and ambient oxides. As we reduce the surface oxides and increase the relative impact of the non-TLS losses, it also becomes

more practical to investigate these mechanisms. Partly motivated by our experimental studies on niobium oxides, Sheridan and Harrelson *et al.* [43,44] have theoretically investigated localized spins in disordered niobium oxides and have shown that such spins can lead to a residual superconducting surface impedance. This is one potential atomic scale mechanism for power-independent interfacial loss in niobium.

Time-dependent fluctuations in superconducting-circuit coherence are a major problem for quantum information science and TLSs are known to cause fluctuations in qubits and resonators [45–48], as are nonequilibrium quasiparticles [49,50], but the role of other non-TLS loss channels remains unclear. Mitigation of surface losses will allow this question to be investigated. We observe, for example, a relative reduction in loss fluctuations for our best resonators (Fig. 19 and Appendix I), which could be an avenue for future investigations.

There have been efforts to isolate different contributions to TLS losses in superconducting circuits going back at least 15 years. Early efforts involving resonator geometries were challenged by scaling relations [37,51] but the SA and MS interfaces were considered the major source of noise based on electrostatic considerations [52]. Recent work with sets of resonators engineered to emphasize different interface contributions [25,53] has shown success. Postfabrication surface modification has been used to increase [25,54] or decrease [53,55] the TLS surface loss. Verjauw *et al.* [56] have recently reported on the TLS loss in niobium surface oxides using an inverse of our approach, by starting with a thin surface oxide on a Nb resonator and correlating loss with oxide growth. Their results are qualitatively similar to ours, which supports the conclusion that, unlike the silicon case, the niobium process and ambient oxides have similar TLS losses. To our knowledge, this work is the first to localize both TLS and non-TLS losses in different materials. We also achieve some of the best performance reported for planar resonators in the quantum regime—a Q_{int} of approximately 6×10^6, corresponding to a resonator lifetime $\tau \sim 0.92$ ms. Verjauw [56] has obtained up to $Q_{\text{int}} \sim 7 \times 10^6$ for $\tau \sim 1.07$ ms. Romanenko [55], using three-dimensional Nb-cavity resonators annealed in ultrahigh vacuum, has obtained a quantum-regime record $Q_{\text{int}} \sim 1.3 \times 10^9$ for $\tau \sim 2.4$ s, with potential applications as quantum memory.

VI. CONCLUSIONS

We robustly achieved state-of-the-art Q values in niobium CPW resonators by removing surface process oxides in devices with pristine metal-substrate interfaces. Selective etching shows that TLS losses arise primarily from exposed dielectric process oxides on our Nb-Si resonators—70% from SiO_x and 23% from NbO_x. We also find that power-independent (non-TLS) losses are concentrated in these oxides—77% from NbO_x and 16% from SiO_x. At most 7% of the losses come from other sources. As we mitigate surface interface losses through selective modification of the interface dielectrics, we arrive in a regime where TLS losses are no longer dominant, which will allow other types of losses in superconducting circuits, such as nonequilibrium quasiparticles, to be investigated in more detail, as well as identification of material hosts for different loss processes. Selective etching could be applied to other superconducting-circuit material systems, for example, to see if other transition-metal oxides host significant non-TLS loss concentrations. Careful control over surfaces and interfaces, such as surface passivation after oxide removal, or changes in fabrication to avoid surface oxidation, can lead to large improvements in quantum circuit performance. Although obtained on resonators, these results are general—they are applicable for qubits and other quantum circuits.

ACKNOWLEDGMENTS

This work was funded by the U.S. Department of Energy, Office of Science, Office of Basic Energy Sciences, Materials Sciences and Engineering Division under Contract No. DE-AC02-05-CH11231, “High-Coherence Multilayer Superconducting Structures for Large Scale Qubit Integration and Photonic Transduction program (QIS-LBNL)” (resonator fabrication, BOE etching, cryogenic characterization, TEM sample preparation). Work at the Molecular Foundry was supported by the U.S. Department of Energy, Office of Science, Office of Basic Energy Sciences under Contract No. DE-AC02-05CH11231 (SEM, TEM, and XPS characterization and data analysis). We acknowledge John Turner for assistance in TEM cross-section preparation, Peter Ercius and Jim Ciston for discussions on EELS data interpretation, and Marie-Paule Delplancke-Ogletree for discussions on inorganic chemistry and metal-oxide etching.

D.F.O., I.S., A.B., A.S., and M.V.P.A. planned the experiments. A.B. and J.M.K. fabricated the resonators. A.B. and E.W. etched resonators. C.B. and M.V.P.A. acquired XPS data. M.V.P.A., C.S., and S.A. prepared cross sections and acquired TEM data. M.V.P.A. acquired SEM and optical images. A.H. and M.A. performed microwave reflectometry. E.W.K. fabricated vacuum assemblies. A.H., A.B., C.B., M.V.P.A., C.S., A.M.S., and D.F.O. analyzed data. D.F.O., I.S., A.S., M.V.P.A., and S.M.G. wrote the manuscript and prepared figures. All authors discussed the results and reviewed the manuscript.

The authors declare no competing financial interests.

APPENDIX A: RESONATOR FABRICATION AND SAMPLE HANDLING

Each (10 × 10)-mm test chip has ten superconducting niobium frequency-multiplexed $\lambda/4$ resonators spanning

6.25–7 GHz. [57]. The gap and width of the CPW waveguide are 10 and 20 μm, respectively. The resonators are weakly coupled to an approximately 50-Ω characteristic impedance feed line with an external quality factor of approximately 700 000 (simulated by ANSYS HFSS software and consistent with measurement).

Samples are fabricated on double-sided polished high-resistivity ($\geq$ 8000 Ω cm) intrinsic silicon $< 100 >$ wafers. Wafers are cleaned in piranha solution (a mixture of sulfuric acid and hydrogen peroxide at 120°C) for 10 min followed by 1 min wet etching in hydrofluoric acid (10:1 solution of 49% HF) to remove the surface contaminants and native oxides. Wafers are inserted into an ultrahigh-vacuum load-locked sputter-deposition system immediately after cleaning (process-chamber base pressure $\leq 5 \times 10^{-8}$ Torr). Nb films (approximately 180 nm) are deposited by magnetron sputtering at room temperature (deposition pressure 1.5 mTorr, time 10 min). A 100-kV Raith electron-beam pattern generator (EBPG 5150) and MicroChem MMA EL-13 copolymer resist are used to pattern the circuits. After patterning, wafers are developed in a 3:1 mixture of IPA:MIBK solution at room temperature, then etched in an inductively coupled reactive-ion etcher (BCl_3-Cl_2 process). After etching, residual resist is removed with Microposit Remover 1165 at 80°C and then wafers are recoated with MMA EL-13 resist for dicing and storage.

The protective resist is stripped from test chips by spraying with acetone for approximately 30 s and then soaking in a beaker partially filled with Microposit Remover 1165 in an 80°C water bath for approximately 12 h. Chips are then sonicated in deionized (DI) water, then acetone, and finally IPA, all at 50°C, before ashing in an oxygen plasma for 1 min. Samples are placed in a custom high-vacuum transport vessel (stainless steel, KF flanges, dry turbo pump) for transfer between the Molecular Foundry at the Lawrence Berkeley National Laboratory (LBNL) (XPS, STEM, and SEM, cross sectioning, BOE etching) and the Siddiqi Laboratories in the Physics Department of the University of California at Berkeley (UCB) (chip fabrication, resist stripping, BOE etching, microwave characterization). No evidence is found of oxide growth or contamination of resist-protected chips during storage.

APPENDIX B: TEM CROSS-SECTION SAMPLE PREPARATION

STEM analysis is performed on cross-section lamella prepared by FIB machining and extracted from resonator chips (Fig. 9) both at the Nb ground plane and along the CPW-resonator waveguide center conductor. An average of three thin sections are obtained from each ten-resonator test chip studied in this work to explore the interface structure and variations with etching time.

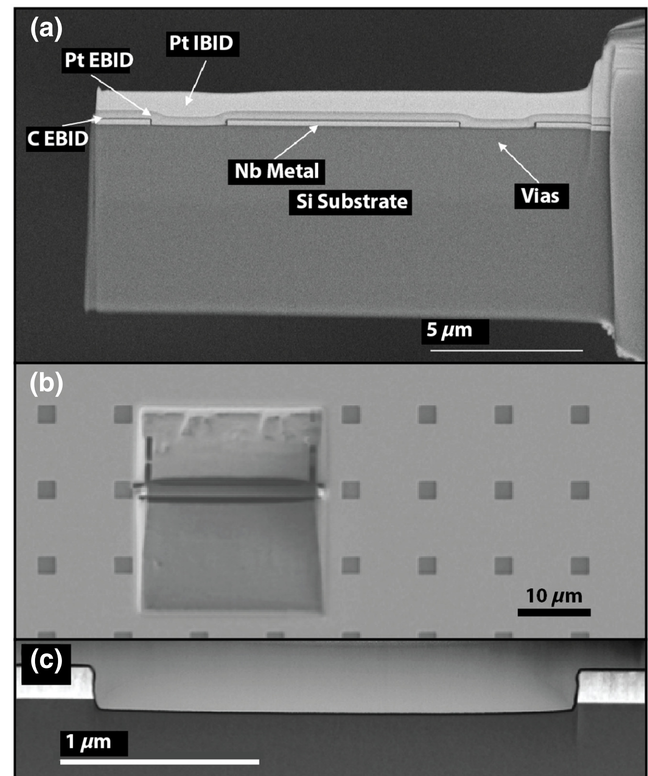

FIG. 9. (a) A SEM image of a TEM cross-section sample prepared by focused-ion-beam (FIB) liftout. The sample lamella are 30–60 nm thick. The sample is protected by an electron-beam-induced deposition (EBID) carbon layer deposited *in situ*, followed by EBID and ion-beam-induced deposition (IBID) Pt layers to protect the sample from Ga^{+} ions during milling. (b) A SEM image of the Nb ground plane after FIB machining and liftout. The cross section cuts through flux traps (square holes or vias) on the ground plane. (c) A STEM image showing etched 180-nm Nb film and over-etching of approximately 75 nm into the Si substrate.

Cross sections are prepared with a FEI Helios G4 UX dual-beam FIB equipped with an EasyLift rotatable needle at the National Center for Electron Microscopy (NCEM) facility at the Foundry. Successive layers of electron-beam-induced carbon, electron-beam-induced platinum, and ion-beam-induced platinum are deposited at the surface of devices for sample protection before liftout and thinning. Additional TEM cross sections are prepared by Outermost Technology using similar instruments and procedures.

APPENDIX C: NIOBIUM GROWTH ON SILICON

The Nb-Si interface, shown in Fig. 10, shows no evidence for an amorphous layer in multiple high-resolution TEM images of our resonators. No interfacial C or O is detected in STEM EELS or EDS.

TEM selected-area diffraction [Fig. 10(b)] shows the epitaxial nucleation of grains in the polycrystalline Nb

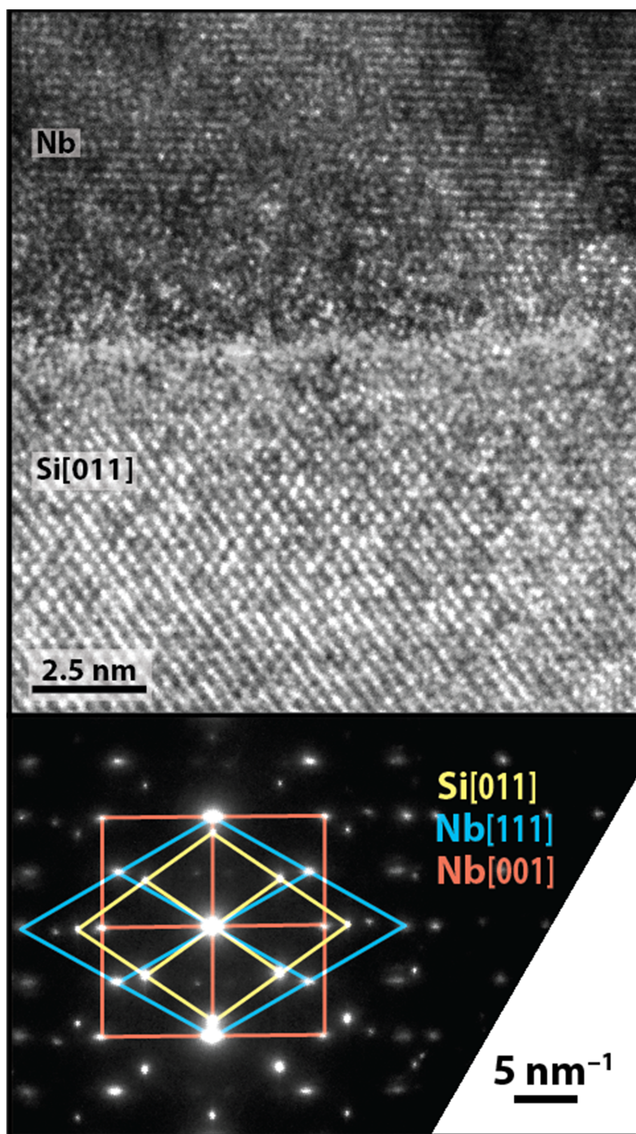

FIG. 10. The niobium-silicon metal-substrate (MS) interface. (a) A high-resolution TEM image shows a clean Nb-Si interface with little to no amorphization and apparent expitaxial niobium-grain nucleation. (b) TEM nanobeam diffraction from a larger region confirms the preferred orientations of Nb grains on Si. Two different Nb grain orientations are observed (see text).

film on the Si(100) substrate. The diffraction data are acquired from a 200-nm-diameter region centered on the interface that includes both the Si substrate and several Nb grains. Similar images are obtained on multiple TEM cross-section samples and on wafers fabricated at different times using similar processes. The incident TEM beam is aligned along the Si[011] "zone axis" of the single-crystal fcc Si lamella. TEM diffraction projects the crystal structures in this plane. In all cases, the bcc Nb(01$\bar{1}$) surface is parallel to the Si(100) wafer surface but two different rotational alignments are observed for individual Nb crystal grains. The yellow lattice in the diffraction pattern is from the Si(011) substrate. The red lattice, with Nb(100) in the cross-section plane, shows the dominant Nb crystal orientation. The blue lattice, with Nb(111) in the cross-section plane, is also observed for some grains. Epitaxial nucleation requires a clean interface—an amorphous interfacial layer would prevent epitaxial growth, since Nb nucleation would no longer be sensitive to the substrate crystallography. Some degree of local disorder, including TLS defects, could still be present at the Nb-Si interface.

APPENDIX D: BOE CHEMISTRY

Buffered oxide etch (BOE) is used in the semiconductor industry to selectively dissolve silicon oxide layers without attacking the substrate wafers [40]. BOE is an aqueous solution of hydrofluoric acid (HF) and ammonium fluoride (NH_4F). Although ammonium fluoride is used as a buffer to stabilize HF solutions in semiconductor manufacturing, it also plays an active role in SiO_2 etch chemistry. Kikuyama *et al.* [58] have studied the process in detail. The main active species are HF_2^- and H^+. Only about 10% of the HF dissociates in aqueous solutions and only about 10% of the fluoride ions form the active HF_2^- species in unbuffered solutions. Ammonium fluoride provides F^- to complex with neutral HF and increase the SiO_2 etch rate. NH_4F alone does not etch SiO_x; some H^+ from HF is required.

Commercial premixed BOE solutions are referred to by ratios such as 5:1, a mixture of 5 volumes of 40 weight percent (wt %) ammonium fluoride (NH_4F) in water to 1 volume of 49 wt % hydrofluoric acid (HF) in water. We use both 5:1 (8.2–8.5 wt% or 4.7 M HF, 9.9 M NH_4F) and 10:1 (4.4–4.7 wt % or 2.5 M HF, 10.8 M NH_4F) BOE solutions. The silicon oxide etch rate has an almost linear dependence on the HF concentration. At 21°C, the etch rates are 1.8 and 0.9 nm/s and they increase by approximately 7% per degree kelvin.

BOE contains HF, *a hazardous material. Etching must be carried out by trained workers with proper personal protective equipment and in a fume hood.*

The etching experiments presented in the main text use 5:1 BOE and are carried out in the QNL. Some additional etching experiments are performed in the Molecular Foundry Nanofabrication Facility at LBNL using 10:1 BOE:

(1) *Etching at UCB*. Four 100-ml cleaned high-density polyethylene (HDPE) beakers are used, one containing 15 ml of J. T. Baker 5:1 CMOS-grade BOE solution. Chips are handled with Teflon tweezers and hand agitated in BOE for the specified interval, removed from the acid and allowed to drip dry, then rinsed for 60 s in each of three consecutive rinse

beakers filled with DI water, and finally blown dry with nitrogen.

(2) *Additional etching at LBNL*. A polytetrafluoroethylene (PTFE) dish is filled with 100 ml of Sigma Aldrich 10:1 BOE and three polypropylene (PP) beakers with 100 ml of house DI water. Chips are handled with PTFE tweezers and laid flat in BOE for the specified interval, followed by rinsing for 60 s in three consecutive beakers. In some cases, a stir bar is used. In some cases, chips have a final rinse in acetone then IPA. The chips are then blown dry with nitrogen.

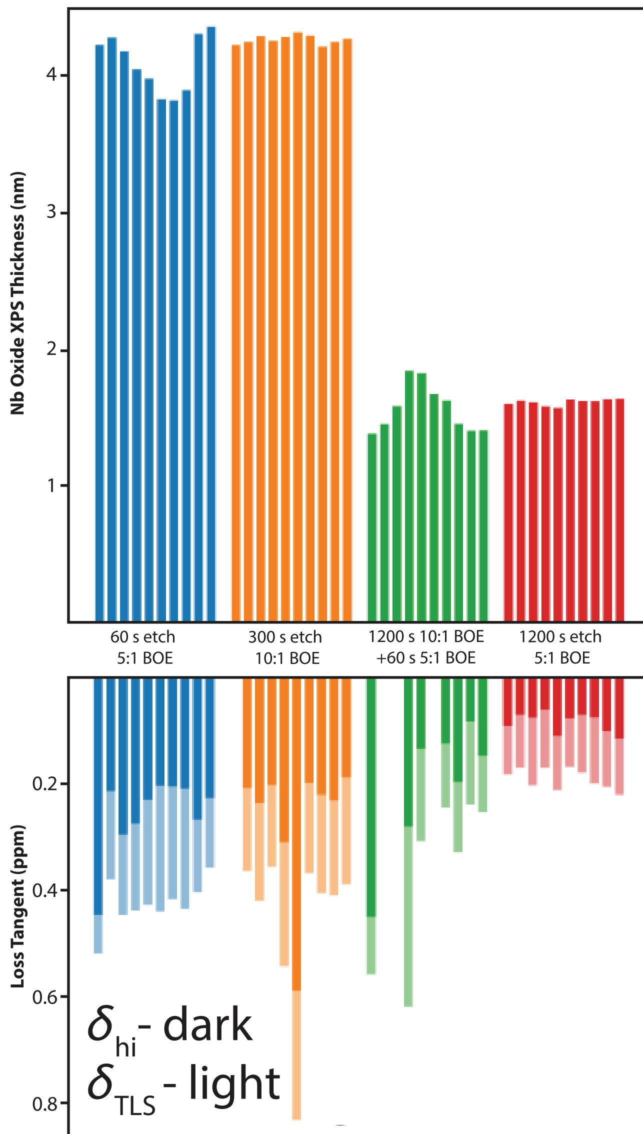

FIG. 11. A comparison of chips etched in 10:1 BOE (blue, red) with chips etched in 5:1 BOE of similar NbO_x thickness. One sample is etched in 10:1 BOE only (green) and the other in both 10:1 and 5:1 BOE (orange).

(3) *BOE 10:1 etching data*. In addition to the data for the standard resonators and the chips etched in 5:1 BOE, we also etch one chip in 10:1 BOE for 5 min and another in 10:1 BOE for 20 min followed by 1 min in 5:1 BOE. Figure 11 compares the results of XPS and microwave reflectometry for the 10:1 chips to a pair of 5:1-etched chips (data also shown in the main text) with similar Nb oxide thicknesses. Except for the difference in etch rates, the loss reductions are consistent with the oxide-thickness changes for 5:1 and 10:1 BOE.

APPENDIX E: NIOBIUM OXIDE ETCHING AND REGROWTH

BOE is not typically used for niobium. Mixtures of hydrofluoric, nitric, and other acids are used to etch the approximately 100-μm damaged metal layers from superconducting 3D Nb-cavity resonators after fabrication from niobium sheets [59,60] and also to remove niobium surface oxides [54]. Nitric acid oxidizes the metallic Nb surface to Nb_2O_5 and then fluoride ions from HF react with the oxide to form water-soluble NbF_5.

Resonator samples are exposed to ambient conditions for approximately 1 h between the end of the etching process and sample mounting in the ADF fridge for loss measurements. Some amount of oxide regrowth may take place during this interval.

The niobium oxide etch rate in BOE, and the Nb and Si oxide regrowth rates, are determined experimentally. The Nb oxidation rate in atmospheric conditions is measured by XPS with an Nb resonator after Ar^+ ion sputter cleaning in the XPS vacuum chamber (Fig. 12). The system pressure with the x-ray source active is $\leq 10^{-7}$ mbar. After 20 min in high vacuum, a submonolayer amount of residual oxygen chemically similar to NbO absorbs on the highly reactive Nb surface. The system is then programmed to move the sample to the airlock and expose it to air for specified intervals before pumping down for the next XPS spectrum. After 1 min of exposure to ambient air, approximately 0.6 nm of niobium oxide forms with Nb_2O_5 and smaller suboxide contributions. After 1 h and 1.1 nm of oxide growth, the ambient oxidation rate drops significantly. No further oxidation is detected after a week of sample storage in low vacuum.

Additional etching experiments are performed on uniform Nb and Si surfaces. A 180-nm Nb film is sputtered onto a Si wafer, which is then plasma ashed for 10 min to produce a process oxide similar to that of the resonators. A clean Si wafer is also plasma ashed. These wafers are cleaved into centimeter-sized pieces and stored in vacuum, then etched for intervals from 15 s to 1680 s. After etching, they are stored in vacuum then transferred into the XPS for analysis, limiting total ambient exposure to a few minutes. The results are shown in

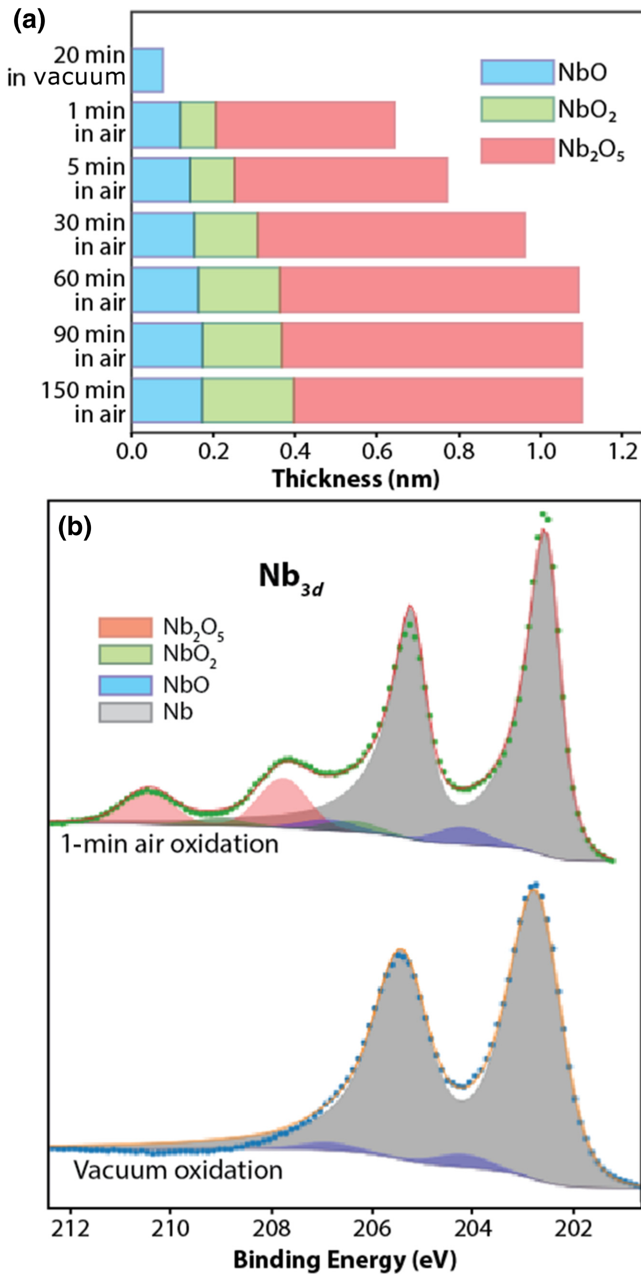

FIG. 12. Reoxidation of sputter-cleaned Nb in high vacuum and air. (a) The growth of Nb_2O_5 and suboxides with air exposure. After 60 min, approximately 1.1 nm of niobium oxide has formed and the oxidation rate has decreased significantly. (b) XPS spectra acquired after the initial formation of a submonolayer amount of NbO in high-vacuum oxidation and after the first air exposure.

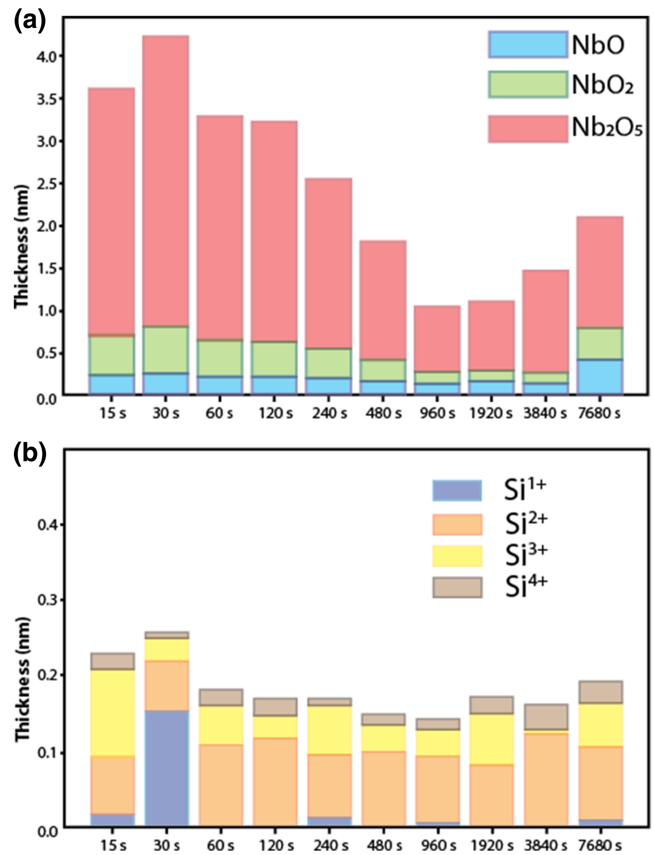

FIG. 13. The etching of Nb (a) and Si (b) process oxides on unpatterned substrates. Moving from left to right, the etch time is doubled for each successive histogram bar. The minimum NbO_x thickness is reached after approximately 1000 s, consistent with oxide removal followed by reoxidation. The SiO_x thickness is approximately a monolayer, independent of the etch time, which is also consistent with the complete removal of the process oxide.

Fig. 13. The original Nb oxide is reduced by half after 480 s in BOE and reaches a minimum thickness of 1 nm between 960 s and 1920 s, suggesting complete removal of original oxide followed by regrowth. The change in the suboxide distribution supports this interpretation. The residual Nb oxide increases for the two longest etch times—which may be an artifact, as there are indications that BOE is starting to attack the acid containers.

In contrast, the SiO_x thickness is uncorrelated with the etch time and is approximately 0.2 nm. This is consistent with complete oxide removal by even brief BOE etching, as expected. The XPS data show almost no Si^{4+} in the oxide, while the original thicker process oxide is primarily Si^{4+}, as shown in Fig. 4(b).

Figure 14 compares the 5:1 BOE niobium process oxide etch rate from the resonator experiments presented in the main text and the experiments in planar films shown in Fig. 13. The measured niobium oxide etch rate is more than 600 times slower than for silicon oxide, approximately 3 pm/s for 5:1 BOE (0.7 pm/s for 10:1 BOE), compared to 1.8 nm/s (0.9 nm/s) for silica [40]. This high selectivity enables sequential etching of SiO_x followed by NbO_x, as well as a gradual reduction of the niobium oxide thickness, which allows direct correlation with resonator losses.

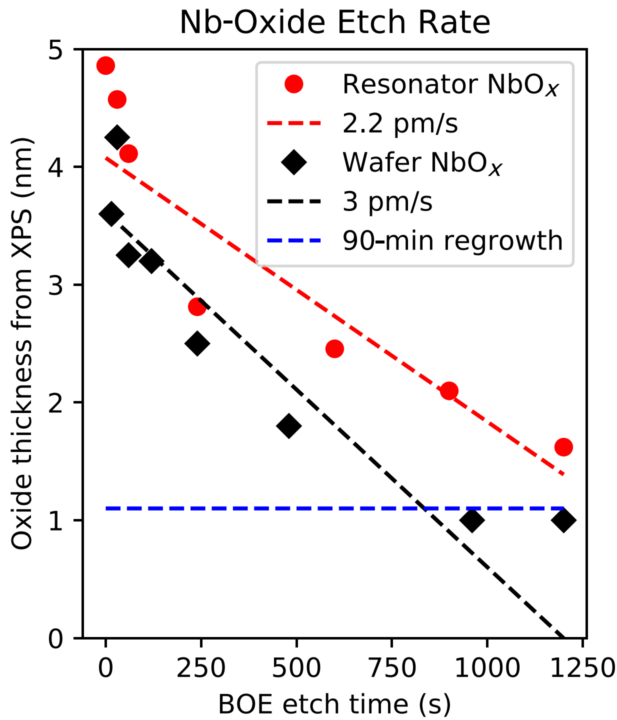

FIG. 14. The NbO_x etch rate in 5:1 BOE from XPS measurements. The resonator experiments discussed in the main text are plotted in red and the data from Fig. 13 in black. The thickness variations at very short etch times reflect sample-to-sample differences in the initial oxide thickness. The resonator process oxide (red) is somewhat thicker than the process oxide simulated by plasma ashing (black).

APPENDIX F: X-RAY PHOTOEMISSION SPECTROSCOPY

XPS is nondestructive and relatively fast, giving averaged interface information over 400-μm regions. XPS can "see through" the surface oxides into the bulk Nb and Si, quantifying the oxide thicknesses and allowing the different Nb and Si oxidation states to be resolved from their chemical shifts [34–36]. TEM, on the other hand, is destructive and relatively slow.

The measured XPS intensities from a stack of layers of different composition can be estimated using the effective-attenuation-length (EAL) model [61]. Each layer is characterized by a thickness t_i, an EAL λ_i, and the relative signal intensity S_i^o for a layer much thicker than λ_i. The λ_i values depend on the photoelectron kinetic energies as well as the layer compositions. Each layer will contribute a signal $S_i = S_i^o e^{1-\lambda_i/t_i}$ and also attenuate the signals from lower layers by $\alpha_i = e^{-\lambda_i/t_i}$. The measured signal from the top layer is $M_1 = S_1$, from the next deeper layer $M_2 = \alpha_1 S_2$, the one below $M_3 = \alpha_1\alpha_2 S_3$, and so on. If the layer stacking order and S_i^o and λ_i values are known, then the t_i can be estimated from the measured XPS intensities, M_i, using the EAL model. Accurate determination of film thicknesses by XPS requires morphological models, which are often inferred; however, here we have direct knowledge of interface chemistry and morphology from TEM [Figs. 3(b) and 16].

Our NbO_x-Nb EAL model consists of four layers from surface to bulk, consistent with the TEM data: Nb_2O_5, NbO_2, NbO, and the Nb substrate. All oxidation states are represented by spin-orbit-split doublets ($\Delta E_{Nb_{3d}} =$ 2.78 eV). The attenuation lengths λ_i and relative sensitivity factors S_i^o for Nb_2O_5 and Nb are calculated using the SESSA scattering-simulation software [62] for our experimental geometry. The calculated $S^o_{Nb_2O_5} : S^o_{Nb}$ ratio is 0.412, which is verified experimentally by comparing Nb_{3d} XPS signals from a thick oxide and clean Nb metal. This ratio is larger than the Nb concentration ratio of 0.343 due to changes in elastic scattering. The calculated $\lambda_{Nb_2O_5}$ value is 1.95 nm but this is rescaled to 1.7 nm to match direct TEM-cross-section measurements. The same λ is used for the thinner suboxide layers and the S_i^o values are scaled with the oxygen concentration, consistent with SESSA results. The suboxide concentrations are proportional to the chemically shifted and attenuated Nb_{3d} peak areas.

For silicon oxide on silicon, we consider four oxide phases represented by spin-orbit split doublets ($\Delta E_{Si_{2p}} =$ 0.63 eV) in order of increasing oxygen concentration: Si, Si_2O, SiO, Si_2O_3, and SiO_2. Extrapolating the density of the intermediate oxides between Si and SiO_2, the relative Si concentrations are 1.0, 0.76, 0.65, 0.58, and 0.53 and the relative silicon S_i^o values are very close. The λ_i values for all phases calculated by SESSA are between 2.81 and 2.87 nm, so we use the SiO_2 literature value of 2.84 nm [63] for all phases. Since we do not have a layer model and since our oxide films are all thinner than λ, the EAL model used for analysis consists of an amorphous SiO_x layer on Si and the suboxide concentrations are proportional to the chemically shifted Si_{2p} peak areas.

X-ray photoelectron spectra are acquired using a Thermo-Fisher K-Alpha$^+$ XPS equipped with a focused monochromatic Al x-ray source, a collection lens with a 30° half-angle acceptance, and a hemispherical analyzer with a multichannel detector at normal incidence to the sample. The x-ray spot size is 200 or 400 μm depending on the data set. A dual-mode monatomic or gas-cluster argon-ion source is used for sputter cleaning and depth profiling. Peak fitting uses the "SKEWVOIGT" line shape for metallic Nb and "PSEUDOVOIGT" for other peaks, using PYTHON software and the LMFIT module [64].

A Shirley inelastic scattering background is used (a Tougaard background gives equivalent results). The Nb_{3d} 0, 2, 4, and 5 oxidation-state energies are 202.3, 204.1, 206.3, and 207.5 eV, respectively. The Si_{2p} 0, 2, 3, and 4 oxidation-state energies are 99.4, 101.8, 102.7, and 103.5 eV, respectively. The Nb:Nb_2O_5 sensitivity ratio in our XPS is experimentally determined by comparing clean-metal and thick-oxide samples.

APPENDIX G: TEM IMAGING, SPECTROSCOPY AND SUPPORTING IMAGES

High-resolution TEM images and EDS elemental maps [Figs. 2, 4(b), 15, and 17] are acquired at 200 kV using a JEOL 2100-F field emission scanning transmission electron microscope equipped with an Oxford high-solid-angle silicon drift detector (SDD) x-ray energy-dispersive spectrometer. A 1-nm-diameter electron-beam probe is used for EDS spectral imaging. EELS is performed at 300 kV in the TEAM I double-aberration-corrected STEM equipped with a high-resolution Continuum Gatan imaging filter (GIF) spectrometer and a $4k \times 4k$ Gatan K3 direct electron detector. EELS spectral imaging maps are acquired using an electron-beam probe 0.1 nm in diameter with 1-eV elastic-peak energy-resolution [Figs. 3(a), 3(b), and 16].

APPENDIX H: RESONATOR CRYO CHARACTERIZATION AND REFLECTOMETRY

There are clear signatures of TLS losses in quantum oscillators [16,22,37]. Resonant TLS losses decrease with temperature as

$$\delta_{\mathrm{TLS}}(T) = \delta^0_{\mathrm{TLS}} \tanh\left(\frac{hf_{\mathrm{res}}}{2k_B T}\right)$$

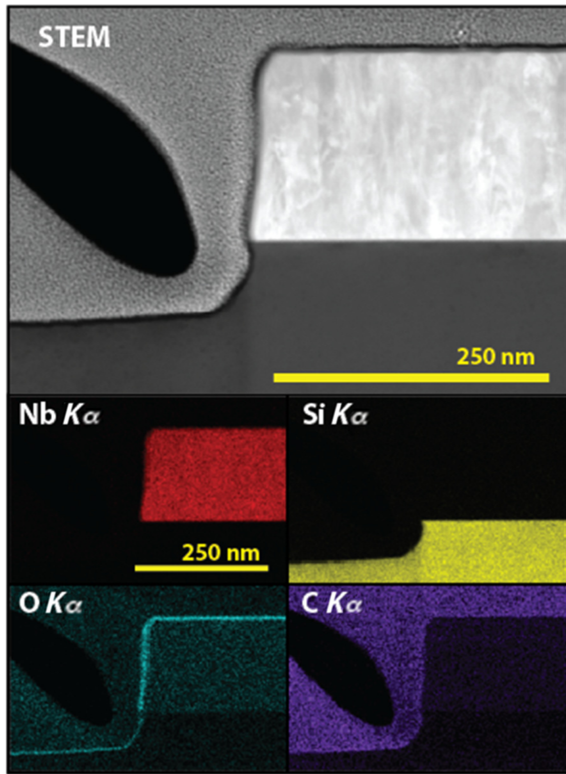

FIG. 15. STEM-EDS cross-section maps of a chip etched for 10 min in 5:1 BOE. Note the reduced oxide thickness at the MA and SA interfaces relative to the standard resonator (Fig. 2). The MS interface is again free of C and O.

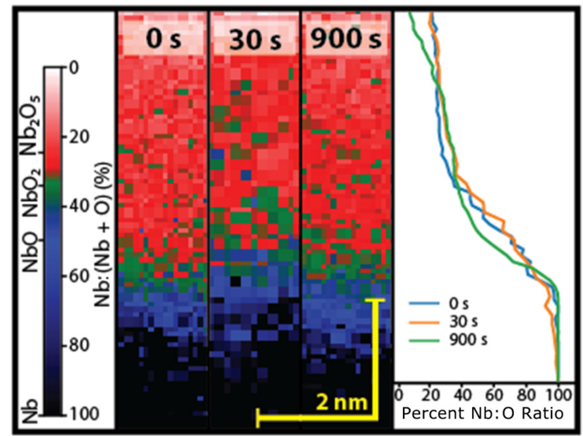

FIG. 16. STEM-EELS data on the niobium oxide MA interface, confirming the variation of the oxide composition with depth. (a) Niobium oxide Nb:(Nb + O) EELS maps as a function of the etch time, showing the spatial distribution of the oxide phases. The morphology of the niobium oxide-metal interface does not change significantly even with extended etching. (b) Depth profiles derived from EELS spectra.

due to thermalization, where δ^0_{TLS} is the TLS loss in the low-temperature low-power limit. In practical circuits, this is a weighted average over different materials hosting TLS. The temperature response of nonresonant TLS

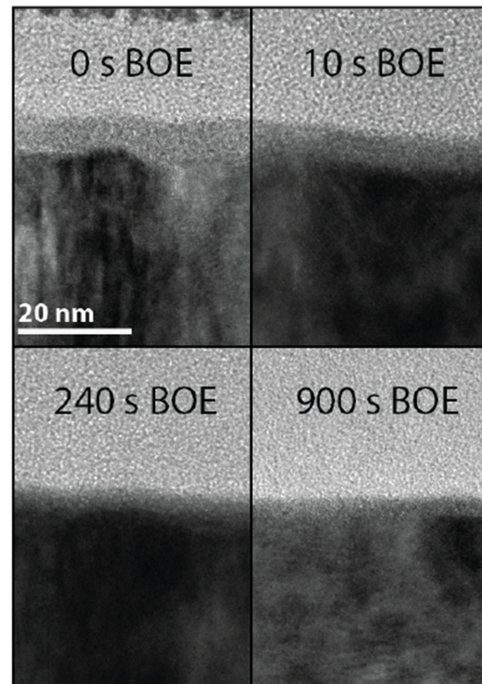

FIG. 17. The evolution of the niobium (MA) interface oxide with the BOE etch time. The NbO_x layer thickness is steadily reduced.

ensembles also changes the dielectric constant, resulting in a temperature-dependent resonant-frequency shift proportional to the TLS density

$$\frac{\Delta f_{\mathrm{res}}}{f_{\mathrm{res}}}(T) = \frac{\delta^0_{\mathrm{TLS}}}{\pi}\left[\mathrm{Re}\ \Psi\left(\frac{1}{2} + \frac{hf_{\mathrm{res}}}{ik_B T}\right) - \log\left(\frac{hf_{\mathrm{res}}}{k_B T}\right)\right],$$

where Ψ is the digamma function. Near a critical photon number n_c, resonant TLSs become increasingly coupled to the quantum microwave circuits and TLS losses decrease as

$$\delta_{\mathrm{TLS}}(T, \langle n\rangle) = \delta_{\mathrm{TLS}}(T)/\sqrt{[1 + (\langle n\rangle/n_c)^{\beta}]}$$

with increasing drive power. For uniform fields, $\beta = 1$. For distributed structures such as a CPW resonator, where electric fields vary with distance from the resonator electrodes and along the length of the resonator, the effective value of β can be smaller but not less than approximately 0.8 for spatially uniform TLS distributions [65]. TLS saturation with increasing electric field strength results in an increase of the resonator quality factor with increasing photon number. These relations, especially saturation, can be modified by TLS-TLS interactions [46,66].

Resonator tests are carried out in a HPD Rainer 103 ADR cryostat with a base temperature of 65 mK. Most measurements are performed at 100 mK. The measurement and shielding details are similar to those in Kreikebaum [67], except that the samples in this work are measured in reflection using a microwave circulator [Fig. 18(c)].

The input power can be converted to the average photon number using $\langle n\rangle = (2/\pi h f_{\mathrm{res}}^2)(Q_T^2/Q_{\mathrm{ext}})P_{\mathrm{in}}$, which can be derived by setting the difference between the input and the reflected power equal to the dissipated power $P_{\mathrm{in}} =$

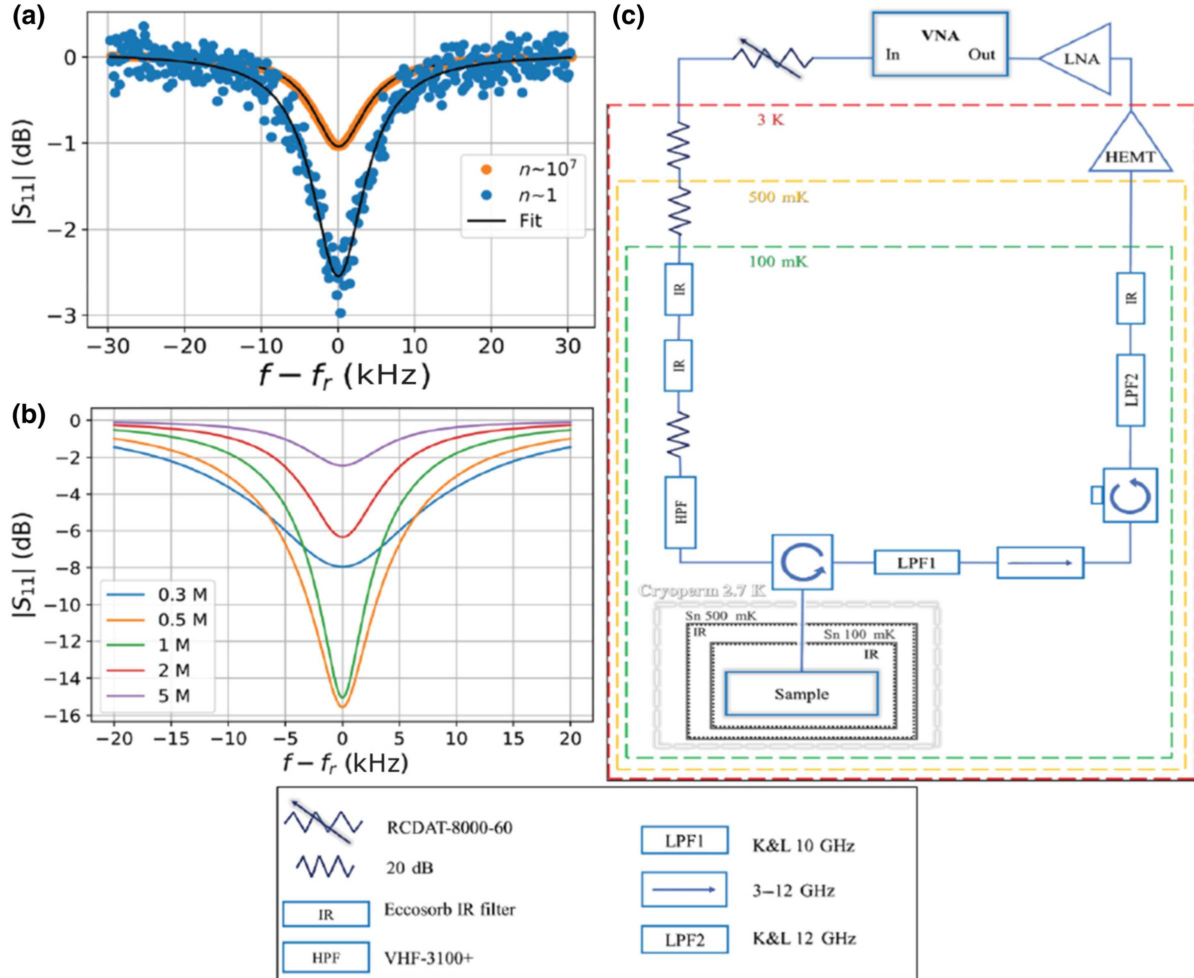

FIG. 18. (a) The reflected signal, after normalization for A and τ, at high power and in the single-photon region for one of the best standard resonators (R6). There is no significant asymmetry in the background. (b) Plots of $|S_{11}|$ calculated for several values of Q_{int} with $Q_{\mathrm{ext}} = 0.7M$. The power dip is maximized for $Q_{\mathrm{int}} \approx Q_{\mathrm{ext}}$. The full width at half maximum increases for $Q_{\mathrm{int}} < Q_{\mathrm{ext}}$, and approaches a minimum for $Q_{\mathrm{int}} > Q_{\mathrm{ext}}$. (c) A schematic of the ADR thermal and radiation shielding and microwave components for reflectometry. The resistor symbols represent thermalized attenuators and IR, HPF, and LPF are infrared, high-pass, and low-pass filters.

$P_{\text{in}}\,|S_{11}|^2 + 2\pi f\, E_{\text{res}}/Q_{\text{int}}$. The input power is estimated from the network-analyzer output, taking into account the attenuation from a RCDAT-8000-60 programmable attenuator and approximately 100 dB of attenuation from the components inside the fridge (measured at room temperature). Figure 18(c) shows a schematic of the setup. More details on the shielding can be found in Kreikebaum *et al.* [67]. The input line is attenuated by 20 dB and thermalized at each stage and passed through homemade absorptive infrared blocking filters (Ecosorb) and a Mini-Circuits VHF-3100+ provides additional filtering.

The output line includes two K&L 10- and 12-GHz low-pass filters, a homemade absorptive infrared blocking filter, 36 dB of isolation from two circulators, 40 dB of gain from a LNC4-8A HEMT at 2.7 K and 36 dB of gain from a MITEQ AFS4-00100800-14-10P-4 amplifier at room temperature.

The acquisition of a $\langle n\rangle \sim 1$ reflection spectrum for a single resonator requires about 8 min for good signal to noise.

The internal quality factor is extracted from the scattering parameters using a vector network analyzer (Rodhe&Schwartz ZVM). At resonance, we observe a sharp attenuation peak, which depends on intrinsic resonator loss and external coupling to the feed line. We design the chip to achieve an external coupling $Q_{\text{ext}} \sim 0.7 \times 10^6$, which is chosen to achieve critical coupling at single-photon excitation for our standard resonators.

The intrinsic quality factor Q_{int} of the resonator reflects the distributed losses across the $\lambda/4$ resonator. The details of the analysis are provided in Ref. [51].

$$\Delta = \frac{Q_T/Q_{\text{ext}}}{1 + 2jQ_T\,\delta f/f_{\text{res}}} e^{i\phi}.$$

We measure the reflected signal when the other end of the feed line is open ($Z_L \to \infty$, $\Gamma_L \to 1$). An intuitive way to understand this configuration is to consider the resonator attenuating the signal twice, first when it passes by as an incoming signal from the left and the second time from the right, after being reflected at the open end of the feed line. So the reflection coefficient S_{11} in the reduced one-port measurement is given by $S_{11} = T_{21}T_{12} \approx 1 - 2\Delta$, where only the linear term in δf is kept and the result is identical to a capacitively coupled resonator at the end of the feed line (one-port model). A more rigorous derivation [68] is to correct for the extended part of the feed line on the network first, by introducing the reflection coefficient Γ_f, and then consider a resonator measured in reflection, the final result being given by

$$S_{11} = \Gamma_f \left(1 - \frac{2\frac{Q}{Q_{\text{ext}}} e^{i\phi}}{1 + 2jQ\frac{\delta f}{f_r}}\right).$$

The extended part of the feed line modifies the coupling, so that if Q_e' is the coupling without an extension, we obtain $Q_e = Q_e'\left[4\Gamma_f/(1+\Gamma_f)^2\right]$. The factor $e^{i\phi}$ is introduced to take into account the impedance mismatch [20,51,68] and this formula is further modified to include a delay time τ and a fixed attenuation level at the output of the network analyzer A, which includes Γ_f:

$$S_{11} = A\, e^{i\tau f}\left(1 - \frac{2Q_T/Q_{\text{ext}}}{1 + 2jQ_T\,\frac{\delta f}{f_{\text{res}}}} e^{i\phi}\right).$$

However, as pointed out in Refs. [20,69], Q_i should be extracted using $1/Q_i = 1/Q_i - \cos\phi/Q_e$, which prevents overestimation of Q_i in the case of a strong coupling mismatch. In our case, we find negligible asymmetry. This can

TABLE I. Tabulated median values of etched chips as a function of the etching conditions. The columns are the single-photon, 10^7 photon, and TLS losses, followed by the niobium and silicon oxide thicknesses determined by XPS. The shaded horizontal row has the combined median properties of the tested standard resonators. The ± ranges are first and third quartiles. Medians and quartiles are used instead of mean and standard deviations since some chips have outliers, individual resonators with values far from the median that skew the mean and standard deviation values. Medians and quartiles are less sensitive outlier effects in small datasets.

Etch time	Single photon (ppm)	10 M photon (ppm)	TLS loss (ppm)	NbO_x (nm)	SiO_x (nm)
No etch 1	0.95 −0.07/+0.42	0.39 −0.13/+0.31	0.62 −0.05/+0.09	5.35 −0.00/+0.01	3.14 −0.19/+0.23
No etch 2	1.08 −0.04/+0.04	0.29 −0.04/+0.04	0.80 −0.03/+0.02	4.38 −0.01/+0.01	2.09 −0.07/+0.05
No etch combined	1.07 −0.12/+0.09	0.31 −0.06/+0.10	0.77 −0.12/+0.04	4.86 −0.47/+0.49	2.39 −0.29/+0.73
30 s	0.47 −0.01/+0.06	0.26 −0.04/+0.02	0.23 −0.03/+0.03	4.57 −0.02/+0.07	0.59 −0.09/+0.04
60 s	0.43 −0.02/+0.01	0.23 −0.02/+0.04	0.16 −0.02/+0.04	4.11 −0.20/+0.15	0.73−0.18/+0.11
10:1 300 s	0.41 −0.04/+0.01	0.22 −0.02/+0.02	0.18 −0.01/+0.02	4.26 −0.02/+0.03	0.19 −0.01/+0.08
240 s	0.36 −0.06/+0.08	0.21 −0.08/+0.06	0.17 −0.00/+0.01	2.81 −0.13/+0.03	2.06 −0.11/+0.05
10:1 1200 s + 5:1 60 s	0.31 −0.06/+0.14	0.15 −0.02/+0.09	0.13 −0.02/+0.03	1.52 −0.10/+0.14	0.97 −0.17/+0.14
600 s	0.28 −0.01/+0.10	0.16 −0.02/+0.04	0.13 −0.01/+0.01	2.45 −0.18/+0.14	0.86 −0.02/+0.12
900 s	0.28 −0.02/+0.05	0.14 −0.01/+0.04	0.13 −0.01/+0.01	2.10 −0.04/+0.07	0.97 −0.03/+0.10
1200 s	0.19 −0.02/+0.01	0.08 −0.00/+0.02	0.11 −0.00/+0.00	1.62 −0.02/+0.01	0.97 −0.03/+0.10

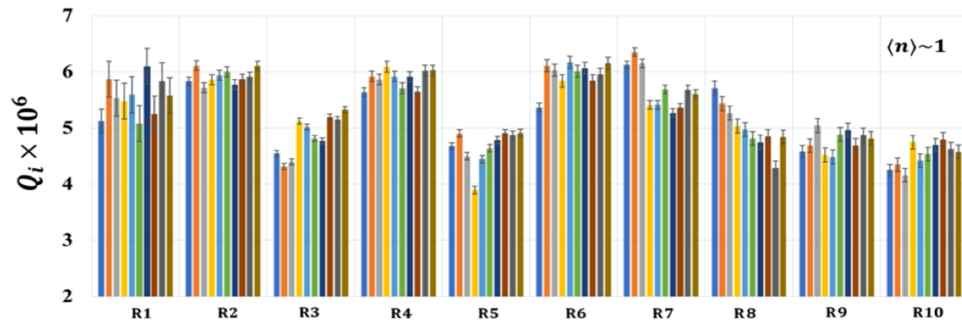

FIG. 19. Repeated measurements of $Q_{\rm int}$ for all resonators (R1–R10) on the 1200-s BOE-etched chip recorded in sequence. The measurement cycle is repeated ten times for 100 total measurements, with each $Q_{\rm int}$ measurement taking 480 s for a total time of 13.5 h. The blue bars are the first set of measurements, the orange the second, etc. The error bars show the fitting uncertainty. R2, R4, and R6 show consistently high performance, while others such as R3 and R8 respectively increase or decrease over time. $\delta_{\rm TLS} \approx \delta_{\rm hi}$ for this chip.

be seen in Fig. 18(a), which shows the fits for R6 at high and low power levels, normalized for A and τ and determined using the LMFIT minimizer package [64]. Figure 6(a) in the main text shows S_{11} fits using these formulas.

APPENDIX I: RESONATOR PERFORMANCE DETAILS

Table I presents the experimental results on the different test chips, reporting median single-photon, high-power, and TLS losses, along with the niobium and silicon oxide thicknesses measured for each resonator on the chip. Figure 19 shows the time-dependent resonator performance. $Q_{\rm int}$ is measured for each resonator in sequence and the sequence is repeated ten times. It is interesting to note that the best-performing resonators (R2, R4, and R6) also have relatively small variations compared to others with higher losses, where $Q_{\rm int}$ tends to increase (R3) or decrease (R8) with time.

[1] M. A. Nielsen and I. Chuang, Quantum computation and quantum information (2002).

[2] N. P. de Leon, K. M. Itoh, D. Kim, K. K. Mehta, T. E. Northup, H. Paik, B. S. Palmer, N. Samarth, S. Sangtawesin, and D. W. Steuerman, Materials challenges and opportunities for quantum computing hardware, Science **372**, 253 (2021).

[3] J. Preskill, Quantum computing in the NISQ era and beyond, Quantum **2**, 79 (2018).

[4] L. B. Nguyen, Y.-H. Lin, A. Somoroff, R. Mencia, N. Grabon, and V. E. Manucharyan, High-Coherence Fluxonium Qubit, Phys. Rev. X **9**, 041041 (2019).

[5] Y. Ding, P. Gokhale, S. F. Lin, R. Rines, T. Propson, and F. T. Chong, in *2020 53rd Annual IEEE/ACM International Symposium on Microarchitecture (MICRO)* (2020), p. 201.

[6] A. Blais, A. L. Grimsmo, S. M. Girvin, and A. Wallraff, Circuit quantum electrodynamics, Rev. Mod. Phys. **93**, 025005 (2021).

[7] M. Kjaergaard, M. E. Schwartz, J. Braumüller, P. Krantz, J. I.-J. Wang, S. Gustavsson, and W. D. Oliver, Superconducting qubits: Current state of play, Annu. Rev. Condens. Matter Phys. **11**, 369 (2020).

[8] R. McDermott, Materials origins of decoherence in superconducting qubits, IEEE Trans. Appl. Supercond. **19**, 2 (2009).

[9] W. D. Oliver and P. B. Welander, Materials in superconducting quantum bits, MRS Bull. **38**, 816 (2013).

[10] M. H. Devoret and R. J. Schoelkopf, Superconducting circuits for quantum information: An outlook, Science **339**, 1169 (2013).

[11] J. M. Martinis, M. H. Devoret, and J. Clarke, Quantum Josephson junction circuits and the dawn of artificial atoms, Nat. Phys. **16**, 234 (2020).

[12] F. Arute *et al.*, Quantum supremacy using a programmable superconducting processor, Nature **574**, 505 (2019).

[13] N. Ofek, A. Petrenko, R. Heeres, P. Reinhold, Z. Leghtas, B. Vlastakis, Y. Liu, L. Frunzio, S. M. Girvin, L. Jiang, M. Mirrahimi, M. H. Devoret, and R. J. Schoelkopf, Extending the lifetime of a quantum bit with error correction in superconducting circuits, Nature **536**, 441 (2016).

[14] A. Blais, R.-S. Huang, A. Wallraff, S. M. Girvin, and R. J. Schoelkopf, Cavity quantum electrodynamics for superconducting electrical circuits: An architecture for quantum computation, Phys. Rev. A **69**, 062320 (2004).

[15] P. Krantz, M. Kjaergaard, F. Yan, T. P. Orlando, S. Gustavsson, and W. D. Oliver, A quantum engineer's guide to superconducting qubits, Appl. Phys. Rev. **6**, 021318 (2019).

[16] J. M. Martinis, K. B. Cooper, R. McDermott, M. Steffen, M. Ansmann, K. D. Osborn, K. Cicak, S. Oh, D. P. Pappas, R. W. Simmonds, and C. C. Yu, Decoherence in Josephson Qubits from Dielectric Loss, Phys. Rev. Lett. **95**, 210503 (2005).

[17] M. Steffen, M. Sandberg, and S. Srinivasan, Recent research trends for high coherence quantum circuits, Supercond. Sci. Technol. **30**, 030301 (2017).

[18] W. A. Phillips, Two-level states in glasses, Rep. Prog. Phys. **50**, 1657 (1987).

[19] C. Müller, J. H. Cole, and J. Lisenfeld, Towards understanding two-level-systems in amorphous solids: Insights

from quantum circuits, Rep. Prog. Phys. **82**, 124501 (2019).

[20] C. R. H. McRae, H. Wang, J. Gao, M. R. Vissers, T. Brecht, A. Dunsworth, D. P. Pappas, and J. Mutus, Materials loss measurements using superconducting microwave resonators, Rev. Sci. Instrum. **91**, 091101 (2020).

[21] I. Siddiqi, Engineering high-coherence superconducting qubits, Nat. Rev. Mater. **6**, 875 (2021).

[22] D. P. Pappas, M. R. Vissers, D. S. Wisbey, J. S. Kline, and J. Gao, Two level system loss in superconducting microwave resonators, IEEE Trans. Appl. Supercond. **21**, 871 (2011).

[23] J. M. Kreikebaum, K. P. O'Brien, A. Morvan, and I. Siddiqi, Improving wafer-scale Josephson junction resistance variation in superconducting quantum coherent circuits, Supercond. Sci. Technol. **33**, 06LT02 (2020).

[24] J. Gao, M. Daal, A. Vayonakis, S. Kumar, J. Zmuidzinas, B. Sadoulet, B. A. Mazin, P. K. Day, and H. G. Leduc, Experimental evidence for a surface distribution of two-level systems in superconducting lithographed microwave resonators, Appl. Phys. Lett. **92**, 152505 (2008).

[25] W. Woods, G. Calusine, A. Melville, A. Sevi, E. Golden, D. K. Kim, D. Rosenberg, J. L. Yoder, and W. D. Oliver, Determining Interface Dielectric Losses in Superconducting Coplanar-Waveguide Resonators, Phys. Rev. Appl. **12**, 014012 (2019).

[26] N. Cabrera and N. F. Mott, Theory of the oxidation of metals, Rep. Prog. Phys. **12**, 163 (1949).

[27] M. D. Henry, S. Wolfley, T. Young, T. Monson, C. J. Pearce, R. Lewis, B. Clark, L. Brunke, and N. Missert, Degradation of superconducting Nb/NbN films by atmospheric oxidation, IEEE Trans. Appl. Supercond. **27**, 1 (2017).

[28] H. D. Ebinger and J. T. Yates, Electron-impact-induced oxidation of Al(111) in water vapor: Relation to the Cabrera-Mott mechanism, Phys. Rev. B Condens. Matter **57**, 1976 (1998).

[29] M. S. Blok, V. V. Ramasesh, T. Schuster, K. O'Brien, J. M. Kreikebaum, D. Dahlen, A. Morvan, B. Yoshida, N. Y. Yao, and I. Siddiqi, Quantum Information Scrambling on a Superconducting Qutrit Processor, Phys. Rev. X **11**, 021010 (2021).

[30] B. K. Mitchell, R. K. Naik, A. Morvan, A. Hashim, J. M. Kreikebaum, B. Marinelli, W. Lavrijsen, K. Nowrouzi, D. I. Santiago, and I. Siddiqi, Hardware-Efficient Microwave-Activated Tunable Coupling between Superconducting Qubits, Phys. Rev. Lett. **127**, 200502 (2021).

[31] D. Bach, H. Störmer, R. Schneider, D. Gerthsen, and J. Verbeeck, EELS investigations of different niobium oxide phases, Microsc. Microanal. **12**, 416 (2006).

[32] R. Tao, R. Todorovic, J. Liu, R. J. Meyer, A. Arnold, W. Walkosz, P. Zapol, A. Romanenko, L. D. Cooley, and R. F. Klie, Electron energy-loss spectroscopy study of metallic Nb and Nb oxides, J. Appl. Phys. **110**, 124313 (2011).

[33] A. Premkumar, C. Weiland, S. Hwang, B. Jäck, A. P. M. Place, I. Waluyo, A. Hunt, V. Bisogni, J. Pelliciari, A. Barbour, M. S. Miller, P. Russo, F. Camino, K. Kisslinger, X. Tong, M. S. Hybertsen, A. A. Houck, and I. Jarrige, Microscopic relaxation channels in materials for superconducting qubits, Commun. Mater. **2**, 1 (2021).

[34] M. V. Kuznetsov, A. S. Razinkin, and E. V. Shalaeva, Photoelectron spectroscopy and diffraction of surface nanoscale NbO/Nb(110) structures, J. Struct. Chem. **50**, 514 (2009).

[35] J. Halbritter, On the oxidation and on the superconductivity of niobium, Appl. Phys. A: Solids Surfaces **43**, 1 (1987).

[36] J. H. Oh, H. W. Yeom, Y. Hagimoto, K. Ono, M. Oshima, N. Hirashita, M. Nywa, A. Toriumi, and A. Kakizaki, Chemical structure of the ultrathin Si_2/Si(100) interface: An angle-resolved Si 2p photoemission study, Phys. Rev. B: Condens. Matter Mater. Phys. **63**, 205310 (2001).

[37] J. Wenner, R. Barends, R. C. Bialczak, Y. Chen, J. Kelly, E. Lucero, M. Mariantoni, A. Megrant, P. J. J. O'Malley, D. Sank, A. Vainsencher, H. Wang, T. C. White, Y. Yin, J. Zhao, A. N. Cleland, and J. M. Martinis, Surface loss simulations of superconducting coplanar waveguide resonators, Appl. Phys. Lett. **99**, 113513 (2011).

[38] C. T. Earnest, J. H. Béjanin, T. G. McConkey, E. A. Peters, A. Korinek, H. Yuan, and M. Mariantoni, Substrate surface engineering for high-quality silicon/aluminum superconducting resonators, Supercond. Sci. Technol. **31**, 125013 (2018).

[39] A. Megrant, C. Neill, R. Barends, B. Chiaro, Y. Chen, L. Feigl, J. Kelly, E. Lucero, M. Mariantoni, P. J. J. O'Malley, D. Sank, A. Vainsencher, J. Wenner, T. C. White, Y. Yin, J. Zhao, C. J. Palmstrøm, J. M. Martinis, and A. N. Cleland, Planar superconducting resonators with internal quality factors above one million, Appl. Phys. Lett. **100**, 113510 (2012).

[40] General Chemical, Electronic Chemicals Group, Technical data: BOE® buffered oxide etchants (2000).

[41] S. E. de Graaf, L. Faoro, L. B. Ioffe, S. Mahashabde, J. J. Burnett, T. Lindström, S. E. Kubatkin, A. V. Danilov, and A. Y. Tzalenchuk, Two-level systems in superconducting quantum devices due to trapped quasiparticles, Sci. Adv. **6**, eabc5055 (2020).

[42] K. Serniak, M. Hays, G. de Lange, S. Diamond, S. Shankar, L. D. Burkhart, L. Frunzio, M. Houzet, and M. H. Devoret, Hot Nonequilibrium Quasiparticles in Transmon Qubits, Phys. Rev. Lett. **121**, 157701 (2018).

[43] E. Sheridan, T. F. Harrelson, E. Sivonxay, K. A. Persson, M. V. P. Altoé, I. Siddiqi, D. Frank Ogletree, D. I. Santiago, and S. M. Griffin, Microscopic theory of magnetic disorder-induced decoherence in superconducting Nb films, arXiv:2111.11684 (2021).

[44] T. F. Harrelson, E. Sheridan, E. Kennedy, J. Vinson, A. T. N'Diaye, M. V. P. Altoé, A. Schwartzberg, I. Siddiqi, D. F. Ogletree, M. C. Scott, and S. M. Griffin, Elucidating the local atomic and electronic structure of amorphous oxidized superconducting niobium films, Appl. Phys. Lett. **119**, 244004 (2021).

[45] C. Müller, J. Lisenfeld, A. Shnirman, and S. Poletto, Interacting two-level defects as sources of fluctuating high-frequency noise in superconducting circuits, Phys. Rev. B Condens. Matter **92**, 035442 (2015).

[46] J. Burnett, L. Faoro, I. Wisby, V. L. Gurtovoi, A. V. Chernykh, G. M. Mikhailov, V. A. Tulin, R. Shaikhaidarov, V. Antonov, P. J. Meeson, A. Y. Tzalenchuk, and T. Lindström, Evidence for interacting two-level systems from the $1/f$ noise of a superconducting resonator, Nat. Commun. **5**, 4119 (2014).

[47] P. V. Klimov *et al.*, Fluctuations of Energy-Relaxation Times in Superconducting Qubits, Phys. Rev. Lett. **121**, 090502 (2018).
[48] J. J. Burnett, A. Bengtsson, M. Scigliuzzo, D. Niepce, M. Kudra, P. Delsing, and J. Bylander, Decoherence benchmarking of superconducting qubits, Npj Quantum Inf. **5**, 54 (2019).
[49] C. D. Wilen, S. Abdullah, N. A. Kurinsky, C. Stanford, L. Cardani, G. D'Imperio, C. Tomei, L. Faoro, L. B. Ioffe, C. H. Liu, A. Opremcak, B. G. Christensen, J. L. DuBois, and R. McDermott, Correlated charge noise and relaxation errors in superconducting qubits, Nature **594**, 369 (2021).
[50] J. M. Martinis, Saving superconducting quantum processors from decay and correlated errors generated by gamma and cosmic rays, Npj Quantum Inf. **7**, 1 (2021).
[51] J. Gao, Ph.D. thesis, California Institute of Technology, 2008.
[52] D. Niepce, J. J. Burnett, M. G. Latorre, and J. Bylander, Geometric scaling of two-level-system loss in superconducting resonators, Supercond. Sci. Technol. **33**, 025013 (2020).
[53] A. Melville, G. Calusine, W. Woods, K. Serniak, E. Golden, B. M. Niedzielski, D. K. Kim, A. Sevi, J. L. Yoder, E. A. Dauler, and W. D. Oliver, Comparison of dielectric loss in titanium nitride and aluminum superconducting resonators, Appl. Phys. Lett. **117**, 124004 (2020).
[54] A. Romanenko and D. I. Schuster, Understanding Quality Factor Degradation in Superconducting Niobium Cavities at low Microwave Field Amplitudes, Phys. Rev. Lett. **119**, 264801 (2017).
[55] A. Romanenko, R. Pilipenko, S. Zorzetti, D. Frolov, M. Awida, S. Belomestnykh, S. Posen, and A. Grassellino, Three-Dimensional Superconducting Resonators at $T < 20$ mK with Photon Lifetimes up to $\{\tau\} = 2$ s, Phys. Rev. Appl. **13**, 034032 (2020).
[56] J. Verjauw, A. Potočnik, M. Mongillo, R. Acharya, F. Mohiyaddin, G. Simion, A. Pacco, T. Ivanov, D. Wan, A. Vanleenhove, L. Souriau, J. Jussot, A. Thiam, J. Swerts, X. Piao, S. Couet, M. Heyns, B. Govoreanu, and I. Radu, Investigation of Microwave Loss Induced by Oxide Regrowth in High-Q Niobium Resonators, Phys. Rev. Appl. **16**, 014018 (2021).
[57] Fabricated in the Quantum Nanoelectronics Laboratory, Department of Physics, University of California at Berkeley.
[58] H. Kikyuama, N. Miki, K. Saka, J. Takano, I. Kawanabe, M. Miyashita, and T. Ohmi, Principles of wet chemical processing in ULSI microfabrication, IEEE Trans. Semicond. Manuf. **4**, 26 (1991).
[59] G. Ciovati, H. Tian, and S. G. Corcoran, Buffered electrochemical polishing of niobium, J. Appl. Electrochem. **41**, 721 (2011).
[60] A. Aspart and C. Z. Antoine, Study of the chemical behavior of hydrofluoric, nitric and sulfuric acids mixtures applied to niobium polishing, Appl. Surf. Sci. **227**, 17 (2004).
[61] P. J. Cumpson and M. P. Seah, Elastic scattering corrections in AES and XPS. II. estimating attenuation lengths and conditions required for their valid use in overlayer/substrate experiments, Surf. Interface Anal. **25**, 430 (1997).
[62] W. Smekal, W. S. M. Werner, and C. J. Powell, Simulation of electron spectra for surface analysis (SESSA): A novel software tool for quantitative auger-electron spectroscopy and x-ray photoelectron spectroscopy, Surf. Interface Anal. **37**, 1059 (2005).
[63] A. Jablonski and C. J. Powell, Effective attenuation lengths for different quantitative applications of x-ray photoelectron spectroscopy, J. Phys. Chem. Ref. Data **49**, 033102 (2020).
[64] M. Newville, R. Otten, A. Nelson, and A. Ingargiola, LMFIT non-linear least-squares minimization and curve-fitting module for PYTHON, Github.
[65] M. S. Khalil, F. C. Wellstood, and K. D. Osborn, Loss dependence on geometry and applied power in superconducting coplanar resonators, IEEE Trans. Appl. Supercond. **21**, 879 (2011).
[66] J. Burnett, T. Lindström, M. Oxborrow, Y. Harada, Y. Sekine, P. Meeson, and A. Ya. Tzalenchuk, Slow noise processes in superconducting resonators, Phys. Rev. B: Condens. Matter Mater. Phys. **87**, 140501(R) (2013).
[67] J. M. Kreikebaum, A. Dove, W. Livingston, E. Kim, and I. Siddiqi, Optimization of infrared and magnetic shielding of superconducting TiN and al coplanar microwave resonators, Supercond. Sci. Technol. **29**, 104002 (2016).
[68] C. Bockstiegel, Y. Wang, M. R. Vissers, L. F. Wei, S. Chaudhuri, J. Hubmayr, and J. Gao, A tunable coupler for superconducting microwave resonators using a nonlinear kinetic inductance transmission line, Appl. Phys. Lett. **108**, 222604 (2016).
[69] M. S. Khalil, M. J. A. Stoutimore, F. C. Wellstood, and K. D. Osborn, An analysis method for asymmetric resonator transmission applied to superconducting devices, J. Appl. Phys. **111**, 054510 (2012).